

ADSORPTION OF HYDROGEN GAS ON POLYMORPHIC
ZIRCONIUM DIOXIDE SURFACES



Miss Monrada Petchmark

จุฬาลงกรณ์มหาวิทยาลัย
CHULALONGKORN UNIVERSITY

A Thesis Submitted in Partial Fulfillment of the Requirements
for the Degree of Master of Science in Chemistry
Department of Chemistry
FACULTY OF SCIENCE
Chulalongkorn University
Academic Year 2021
Copyright of Chulalongkorn University

การดูดซับแก๊สไฮโดรเจนบนผิวพหุสัณฐานเซอร์โคเนียมไดออกไซด์



วิทยานิพนธ์นี้เป็นส่วนหนึ่งของการศึกษาตามหลักสูตรปริญญาวิทยาศาสตรมหาบัณฑิต

สาขาวิชาเคมี ภาควิชาเคมี

คณะวิทยาศาสตร์ จุฬาลงกรณ์มหาวิทยาลัย

ปีการศึกษา 2564

ลิขสิทธิ์ของจุฬาลงกรณ์มหาวิทยาลัย

Thesis Title	ADSORPTION OF HYDROGEN GAS ON POLYMORPHIC ZIRCONIUM DIOXIDE SURFACES
By	Miss Monrada Petchmark
Field of Study	Chemistry
Thesis Advisor	Professor VITHAYA RUANGPORNVISUTI, Dr.rer.nat.

Accepted by the FACULTY OF SCIENCE, Chulalongkorn University in Partial Fulfillment of the Requirement for the Master of Science

 Dean of the FACULTY OF SCIENCE
 (Professor POLKIT SANGVANICH, Ph.D.)

THESIS COMMITTEE

 Chairman
 (Professor THAMMARAT AREE, Dr.rer.nat.)

 Thesis Advisor
 (Professor VITHAYA RUANGPORNVISUTI, Dr.rer.nat.)

 Examiner
 (Associate Professor VIWAT VCHIRAWONGKWIN, Dr.rer.nat.)

 External Examiner
 (Associate Professor Korakot Navakhun, Ph.D.)



จุฬาลงกรณ์มหาวิทยาลัย
 CHULALONGKORN UNIVERSITY

มนรดา เพชรมาก : การดูดซับแก๊สไฮโดรเจนบนผิวพหุสัณฐานเซอร์โคเนียมไดออกไซด์. (ADSORPTION OF HYDROGEN GAS ON POLYMORPHIC ZIRCONIUM DIOXIDE SURFACES) อ.ที่ปรึกษาหลัก : ศ. ดร.วิทยา เรืองพรวิสุทธ์

การดูดซับแก๊สไฮโดรเจนบนผิวพหุสัณฐานเซอร์โคเนียมไดออกไซด์ ประกอบไปด้วย โครงสร้างชนิดคิวบิก(111), เทตระโกนอล(101) และโมโนคลินิก(111) ได้รับการคำนวณด้วยวิธี ฟิรูดิกคิเอฟที่ ความเสถียรของโครงสร้างผิวเซอร์โคเนียมไดออกไซด์แบบสมบูรณพบว่ามีลำดับดังนี้ $c\text{-ZrO}_2(111) > t\text{-ZrO}_2(101) > m\text{-ZrO}_2(111)$ และแบบมีช่องว่างของออกซิเจนอะตอมมีความเสถียรของโครงสร้างตามลำดับดังนี้ $[c\text{-ZrO}_2(111)+V_O] > [t\text{-ZrO}_2(101)+V_O] > [m\text{-ZrO}_2(111)+V_O]$ ความสามารถในการดูดซับแก๊สไฮโดรเจนบนผิวแบบสมบูรณและแบบมีช่องว่างของออกซิเจนอะตอมพบว่ามีลำดับดังนี้ $[c\text{-ZrO}_2(111)+V_O] (\Delta E_{\text{ads}} = -4.13 \text{ eV}) > [m\text{-ZrO}_2(111)+V_O] (\Delta E_{\text{ads}} = -3.31 \text{ eV}) > [t\text{-ZrO}_2(101)+V_O] (\Delta E_{\text{ads}} = -2.91 \text{ eV}) > c\text{-ZrO}_2(111) (\Delta E_{\text{ads}} = -1.89 \text{ eV}) > m\text{-ZrO}_2(111) (\Delta E_{\text{ads}} = -1.67 \text{ eV}) > t\text{-ZrO}_2(101) (\Delta E_{\text{ads}} = -0.27 \text{ eV})$ โครงสร้างผิว $c\text{-ZrO}_2(111)$ ที่ถูกเจือด้วยธาตุแลนทาไนด์ได้รับการคำนวณ และความสามารถในการดูดซับแก๊สไฮโดรเจนบนผิว $\text{Eu-}[c\text{-ZrO}_2(111)+V_O] (\Delta E_{\text{ads}} = -0.80 \text{ eV})$ มีค่ามากกว่าการดูดซับบนผิว $\text{Ce-}[c\text{-ZrO}_2(101)] (\Delta E_{\text{ads}} = -0.21 \text{ eV})$. โครงสร้างผิวเซอร์โคเนียมไดออกไซด์แบบมีช่องว่างของออกซิเจนอะตอมพบว่ามีศักยภาพในการเป็นวัสดุกักเก็บแก๊สไฮโดรเจน และผิวเซอร์โคเนียมไดออกไซด์ชนิด $[t\text{-ZrO}_2(101)+V_O]$, $[m\text{-ZrO}_2(111)+V_O]$ และ $m\text{-ZrO}_2(111)$ พบว่าสามารถใช้เป็นวัสดุตรวจจับแก๊สไฮโดรเจน โดยการตรวจวัดความต้านทานไฟฟ้า



สาขาวิชา เคมี
ปีการศึกษา 2564

ลายมือชื่อนิสิต
ลายมือชื่อ อ.ที่ปรึกษาหลัก

6270093823 : MAJOR CHEMISTRY

KEYWORD: Polymorphic ZrO₂ surfaces, Hydrogen storage, Hydrogen adsorption energy, Periodic DFT

Monrada Petchmark : ADSORPTION OF HYDROGEN GAS ON POLYMORPHIC ZIRCONIUM DIOXIDE SURFACES. Advisor: Prof. VITHAYA RUANGPORNVISUTI, Dr.rer.nat.

Adsorption of hydrogen gas on polymorphic zirconium dioxide (ZrO₂) surfaces including cubic, tetragonal and monoclinic phase denoted by c-ZrO₂(111), t-ZrO₂(101) and m-ZrO₂(111), respectively has been investigated using the periodic density functional theory (DFT) calculation. The stabilities of perfect and oxygen vacancy defective ZrO₂ surfaces are in orders: c-ZrO₂(111) > t-ZrO₂(101) > m-ZrO₂(111) and [c-ZrO₂(111)+V_O] > [t-ZrO₂(101)+V_O] > [m-ZrO₂(111)+V_O], respectively. The abilities of hydrogen adsorption on perfect and oxygen vacancy defective ZrO₂ surfaces are in orders: [c-ZrO₂(111)+V_O] ($\Delta E_{\text{ads}} = -4.13$ eV) > [m-ZrO₂(111)+V_O] ($\Delta E_{\text{ads}} = -3.31$ eV) > [t-ZrO₂(101)+V_O] ($\Delta E_{\text{ads}} = -2.91$ eV) > c-ZrO₂(111) ($\Delta E_{\text{ads}} = -1.89$ eV) > m-ZrO₂(111) ($\Delta E_{\text{ads}} = -1.67$ eV) > t-ZrO₂(101) ($\Delta E_{\text{ads}} = -0.27$ eV). The lanthanide-doped c-ZrO₂(111) surfaces were obtained and exhibit hydrogen adsorption stability. Hydrogen adsorption ability on Eu-[c-ZrO₂(111)+V_O] ($\Delta E_{\text{ads}} = -0.80$ eV) is higher than on Ce-[c-ZrO₂(101)] ($\Delta E_{\text{ads}} = -0.21$ eV). The oxygen vacancy defective polymorphic ZrO₂ surfaces exhibit a high potential for hydrogen-storage materials. The [t-ZrO₂(101)+V_O], [m-ZrO₂(111)+V_O] and m-ZrO₂(111) surface types have been recommended as hydrogen-sensing materials via electrical resistance measurement.



Field of Study: Chemistry
Academic Year: 2021

Student's Signature
Advisor's Signature

ACKNOWLEDGEMENTS

First of all, I would like to express my deepest appreciation to my advisor Professor Dr. Vithaya Ruangpornvisuti for his supervision, encouragement, and consistent support during the working on this research. His constructive suggestion and plentiful experience have inspired me in the time of my academic research.

Furthermore, I especially grateful to thesis committee members: Professor Dr. Thammarat Aree, Associate Professor Dr. Viwat Vchirawongkwin, and Associate Professor Dr. Korakot Navakhun who discuss and suggest on this research. This thesis has been success through my encounters and answer their question with all committee members.

I would like to thank member in Prof. Dr. Vithaya Ruangpornvisuti's lab who encourage and support me to do this research successful. Thank for supporting and encouraging to me throughout this work. I will not get this far without their help.

Thank also to the South Korean boy band including BTS, TOMORROW BY TOGETHER, ENHYPHEN, and SF9 for their good songs that have been healing my stress occurred during working on this research. Their motivation to be the good artist have been pushed me to have intention to accomplish this thesis.

My thanks also go out to my friends who encourage and heal me when I am so tired. Thank you, my friends who give the good advice and listen to my problem, when I am in bad time.

Last but not least, I would like to heartfelt thank my family who are important in my life. Thank you for always believing in me and giving the good advice to me. Without hope from my parents that they had given to me, this thesis would not have been successful. So with due regards, I express my gratitude to them.

Monrada Petchmark

TABLE OF CONTENTS

	Page
ABSTRACT (THAI)	iii
ABSTRACT (ENGLISH).....	iv
ACKNOWLEDGEMENTS	v
TABLE OF CONTENTS.....	vi
LIST OF TABLES	viii
LIST OF FIGURES	x
LIST OF ABBREVIATIONS AND SYMBOLS	xi
CHAPTER I INTRODUCTION.....	1
1.1 Background.....	1
1.2 Zirconium dioxide (ZrO ₂).....	2
1.3 Literature reviews	7
1.4 Objectives	10
CHAPTER II THEORETICAL BACKGROUND.....	11
2.1 <i>Ab Initio</i> method	11
2.2 Density functional theory (DFT) method	12
2.2.1 The Kohn-Sham equations	13
2.2.2 The functionals E_x and E_c	14
2.2.3 Generalized-gradient (GGA) Functionals	15
2.3 Basis sets.....	16
2.3.1 Gaussian basis set.....	16
2.3.2 Minimal Basis set	17
2.3.3 Split-Valence Basis sets	18
2.3.4 Polarization Basis sets	18
2.3.5 Diffuse Basis sets	19
2.3.6 Effective Core Potentials (Pseudopotentials).....	19

2.4 Mülliken population analysis.....	20
2.5 Band structure	21
CHAPTER III COMPUTATIONAL DETAILS	23
3.1 Polymorphic Zirconium dioxide structures optimization	23
3.2 Adsorption of hydrogen molecule on the polymorphic ZrO ₂ surfaces.....	25
3.3 The electrical conductivity	25
3.4 The bond strength	26
CHAPTER IV RESULTS AND DISCUSSION	27
4.1 Surface structures and relative stabilities of polymorphic ZrO ₂ surfaces.....	27
4.2 Adsorption of a single hydrogen molecule on polymorphic ZrO ₂ surfaces.....	29
4.3 The charge transfers process on adsorption structures of polymorphic ZrO ₂ surfaces	33
4.4 The difference of bandgap and electrical conductivity and resistivity of a hydrogen molecule adsorption on polymorphic ZrO ₂ surfaces.....	38
4.5 Bond strengths of adsorption of a hydrogen molecule on polymorphic ZrO ₂ surfaces	40
4.6 Hydrogen adsorption on Lanthanide-doped c-ZrO ₂ (111) surface	42
CHAPTER V CONCLUSIONS	49
REFERENCES	50
VITA.....	62

LIST OF TABLES

	Page
Table 1.1 Chemical composition of baddeleyite in various type of rocks.....	3
Table 1.2 Physical Properties of Zirconia.....	5
Table 4.1 Total and relative energies of the c-ZrO ₂ (111), t-ZrO ₂ (101), and m-ZrO ₂ (111) surfaces and their oxygen vacancy defective surfaces.....	29
Table 4.2 Adsorption energies of a hydrogen molecule on the c-ZrO ₂ (111), t-ZrO ₂ (101), and m-ZrO ₂ (111) surfaces and their oxygen vacancy defect.....	33
Table 4.3 The partial charge of the Zr adsorption-site atom, and its change after adsorption. of a hydrogen molecule on the c-ZrO ₂ (111), t-ZrO ₂ (101), and m-ZrO ₂ (111) surfaces and their oxygen vacancy defect.....	34
Table 4.4 Partial Mülliken–charges of selected atoms on the pristine ZrO ₂ surfaces, their H ₂ adsorption complexes, and changes of their charges.....	36
Table 4.5 Partial Mülliken–charges of selected atoms on the oxygen vacancy defective ZrO ₂ surfaces, their H ₂ adsorption complexes, and changes of their charges.....	37
Table 4.6 Energy gaps and sensitivity of electrical conductivity and resistivity of adsorption of hydrogen molecule on pristine and oxygen vacancy defective polymorphic ZrO ₂ surfaces.....	39
Table 4.7 Energy gaps of the c-ZrO ₂ (111), t-ZrO ₂ (101), and m-ZrO ₂ (111) surfaces compared with their oxygen vacancy defect in terms of energy–gap change.....	40
Table 4.8 Zr-H bond strengths of a hydrogen molecule on oxygen vacancy defective ZrO ₂ surfaces.....	41
Table 4.9 Total energies of the c-ZrO ₂ (111), Ce-[c-ZrO ₂ (101)], [c-ZrO ₂ (111)+Vo] and Eu-[c-ZrO ₂ (111)+Vo] surfaces.....	44

Table 4.10 Adsorption energies of single H ₂ molecules on the c-ZrO ₂ (111), Ce-[ZrO ₂ (101)], [c-ZrO ₂ (111)+Vo] and Eu-[c-ZrO ₂ (111)+Vo] surfaces, energy gaps, Mülliken charge of the dopant and Zr adsorption-site atoms and their change after hydrogen adsorption.....	46
Table 4.11 Partial Mülliken–charges of selected atoms on the [c-ZrO ₂ (111)] and Ce-[c-ZrO ₂ (111)] surfaces, their H ₂ adsorption complexes and changes of their charges.	47
Table 4.12 Partial Mülliken–charges of selected atoms on the [c-ZrO ₂ (111)+Vo] and Eu-[c-ZrO ₂ (111)+Vo] surfaces, their H ₂ adsorption complexes and changes of their charges.....	48



LIST OF FIGURES

	Page
Figure 1.1 Unit cell of cubic, tetragonal, and monoclinic ZrO_2	4
Figure 1.2 Calculated PBE0/ $Zr^{ECP}-O^{ECP}$ band structure and total and Zr-4d, Zr-4p, O-2s, O-2p projected DOS of cubic, tetragonal, and monoclinic ZrO_2	4
Figure 4.1 Structures of c- $ZrO_2(111)$, t- $ZrO_2(101)$ and m- $ZrO_2(111)$ surfaces.....	27
Figure 4.2 Structures of [c- $ZrO_2(111)+V_o$], [t- $ZrO_2(101)+V_o$], and [m- $ZrO_2(111)+V_o$] surfaces.....	28
Figure 4.3 Optimized structures of hydrogen molecule adsorption on c- $ZrO_2(111)$, t- $ZrO_2(101)$ and m- $ZrO_2(111)$	30
Figure 4.4 Optimized structures of hydrogen molecule dissociative adsorption on [c- $ZrO_2(111)+V_o$], [t- $ZrO_2(101)+V_o$], and [m- $ZrO_2(111)+V_o$] surfaces..	31
Figure 4.5 Optimized structures of hydrogen molecule adsorption on c- $ZrO_2(111)$ and Ce-[c- $ZrO_2(111)$]	43
Figure 4.6 Optimized structures of hydrogen molecule adsorption on [c- $ZrO_2(111)+V_o$] and Eu-[c- $ZrO_2(111)+V_o$]	45

LIST OF ABBREVIATIONS AND SYMBOLS

\AA	Angstrom
BS	Bond strengths
$c\text{-ZrO}_2$	Cubic Zirconium dioxide
$[c\text{-ZrO}_2(111)+V_o]$	Oxygen vacancy defective cubic Zirconium dioxide(111) surface
$Ce\text{-}[c\text{-ZrO}_2(111)]$	Cerium-doped cubic Zirconium dioxide(111) surface
DFT	Density functional theory
ECP	Effective core potentials
E_g	Energy gap
$Eu\text{-}[c\text{-ZrO}_2(111)+V_o]$	Europium-doped oxygen vacancy defective cubic Zirconium dioxide(111) surface
ΔE_{ads}^{pris}	Adsorption energy on pristine ZrO_2 surfaces
ΔE_{ads}^{def}	Adsorption energy on oxygen vacancy defective ZrO_2 surfaces
\hat{H}	Hamiltonian operator
HF	Hartree-Fock
$m\text{-ZrO}_2$	Monoclinic Zirconium dioxide
$[m\text{-ZrO}_2(111)+V_o]$	Oxygen vacancy defective Monoclinic Zirconium dioxide(111) surface
PBE	Perdew-Becke-Ernzerhof
$S_{\sigma}^{\%}$	Sensitivity of electrical conductivity
$S_{\rho}^{\%}$	Sensitivity of electrical resistivity
$t\text{-ZrO}_2$	Tetragonal Zirconium dioxide
$[t\text{-ZrO}_2(101)+V_o]$	Oxygen vacancy defective tetragonal Zirconium dioxide(101) surface
ZrO_2	Zirconium dioxide
ψ	Wave function

σ	Electrical conductivity
ρ	Electrical resistivity



CHAPTER I

INTRODUCTION

1.1 Background

Hydrogen has been suggested as clean and sustainable energy. Hydrogen is the simplest and most abundant element in the universe, especially it is eco-friendly, high-energy density and renewable thus hydrogen storage is the most important to apply in energy industries [1-4]. Nowadays, there are many materials which use for store hydrogen. Transition metal oxides (TMOs) have been broadly investigated materials for hydrogen storage materials [5-8]. Zirconium dioxide (ZrO_2) is one of transition metal oxides which broadly studied in many fields such as ceramics [9], electro-optical materials [10], biomedical materials [11], electrolyte in solid oxide fuel cells (SOFCs) [12], gas sensor [13] and catalysts [14-17]. The distinguished properties of ZrO_2 include mechanical strength, thermal stability, low corrosion potential, toughness, wide band gap, and biocompatibility contribute ZrO_2 to be an attractive material to apply in many fields.

ZrO_2 consists of three main polymorphs including cubic, tetragonal, and monoclinic. The cubic, tetragonal, and monoclinic zirconia ($c-ZrO_2$, $t-ZrO_2$, $m-ZrO_2$) were studied, and the bandgap of the $t-ZrO_2$ larger than $m-ZrO_2$ by 0.35 eV was found [18]. The acid-base characteristics of surfaces of $t-ZrO_2$ and their CO and CO_2 adsorption were studied [19]. Structural parameters, elastic, electronic, bonding, and optical properties of $m-ZrO_2$ were investigated [20]. The structural, mechanical, and thermodynamic properties of $c-ZrO_2$, $t-ZrO_2$, $m-ZrO_2$ were investigated by DFT [21]. Structural, electronic, optical, and elastic properties of ZrO_2 were investigated using the DFT method [22]. Electronic, optical, and elastic properties of $c-ZrO_2$ were studied [23]. The band structure, optical absorption, and emission spectra of ZrO_2 were analyzed [24], and optical spectra of the ZrO_2 crystal containing oxygen vacancy based on the DFT were studied [25]. The oxygen vacancy defective surface of ZrO_2 as the blue luminescence centers was studied [26].

The adsorptions of small molecules, including H₂, on the c-ZrO₂(110) surface were studied [27]. The formation of protonated forms of c-ZrO₂ was studied [28]. Hydrogen interstitials in pristine m-ZrO₂ and hydrogen mono- and co-occupying oxygen vacancy were investigated [29].

Doping on zirconia has been widely studied for catalyst, energy storage and biomedical applications [30-34]. Nowadays, rare earth elements doped ZrO₂ materials have been broadly studied. These studies show that rare earth elements doping affect to physical properties, optical properties, and crystal structure of materials [35-37]. Ce-doped ZrO₂ materials have been synthesized that exhibit monoclinic and tetragonal phase. Ce doping induced a modification of the ratio between tetragonal and monoclinic phase, increasing percentage of Ce doping can increase tetragonal phase [38, 39]. Ce-doped ZrO₂ nanophosphors was synthesized by co-precipitation method which is found to show in fluorite cubic structure with unit cell to be $a=5.1280 \text{ \AA}$. The Ce-doped-ZrO₂ nanophosphors showed photoluminescence emission spectra around 486 nm and 532 nm, and at 236 nm and 346 nm when it is excited which can be suggest to be blue-green light emitting materials [40]. Eu-doped ZrO₂ materials have been synthesized which have cubic fluorite structure ($Fm\bar{3}m$) [41, 42]. Oxygen vacancies are observed which Eu related to the number of surface oxygen vacancies induced [41].

The structural and electronic properties of the clean c-ZrO₂ (111) surface, its oxygen vacancy defective surface, and yttria-stabilized zirconia (YSZ) were studied using DFT methods in a periodic approach [43]. The structure and stability of m-ZrO₂ were studied and found that m-ZrO₂ (111) and m-ZrO₂ ($\bar{1}11$) surfaces were dominant indices [44]. The influence of the surface oxygen vacancy (V_o) of YSZ compared with the bare YSZ(111) was investigated [45]. Nevertheless, a study of H₂ adsorption on pristine c-ZrO₂, t-ZrO₂, and m-ZrO₂ surfaces and their oxygen vacancy defective surfaces was hardly found.

1.2 Zirconium dioxide (ZrO₂)

Zirconium dioxide (Zirconia; ZrO₂) can be essentially found from mineral baddeleyite. Baddeleyite is not commonly natural mineral, but it is in trace phase in

various type of rocks. Chemical compositions of baddeleyite in various type of rocks are shown in Table 1.1. ZrO_2 is prevalent in baddeleyite, 87–99% by weight [46] and it exists in the monoclinic phase [47].

Table 1.1 Chemical composition (wt%) of baddeleyite in various type of rocks [46]

	Lunar basalts			Mafic-ultramafic rocks			Metacarbonatites		
	Ave.	Min.	Max.	Ave.	Min.	Max.	Ave.	Min.	Max.
Nb_2O_5	0.8	0.6	1.1	0.4	–	–	0.4	0.2	0.9
SiO_2	0.2	0.1	0.3	0.1	0.0	0.2	–	–	–
ZrO_2	92.5	87.2	94.8	97.0	92.5	98.7	96.9	95.0	99.0
TiO_2	3.2	1.3	8.0	1.1	0.1	2.6	0.7	0.0	1.7
HfO_2	2.0	1.6	2.6	1.5	0.9	2.2	1.8	1.0	2.5
Al_2O_3	0.3	0.1	0.6	0.1	0.0	0.2	–	–	–
Cr_2O_3	0.2	0.1	0.3	0.1	0.0	0.2	–	–	–
Y_2O_3	1.4	1.2	1.5	0.1	0.0	0.3	0.2	0.0	0.3
MgO	0.1	0.0	0.2	0.1	0.0	0.3	–	–	–
CaO	0.3	0.1	0.6	0.1	0.0	0.4	0.4	0.0	0.9
MnO	0.1	0.0	0.2	<0.1	0.0	0.1	–	–	–
FeO	1.1	0.4	2.1	0.8	0.0	2.2	0.6	0.1	2.2

ZrO_2 exists in three stable polymorphs including cubic (c- ZrO_2), tetragonal (t- ZrO_2), and monoclinic (m- ZrO_2) forms. Unit cell structures of cubic, tetragonal, and monoclinic are shown in Figure 1.1. Monoclinic ZrO_2 (space group $P2_1/c$) is abundant in baddeleyite and is stable at room temperature [48]. Upon heating, the monoclinic-tetragonal phase transition occurs at 1000~1200°C. Then tetragonal (space group $P4_2/nmc$) transforms to cubic (space group $Fm\bar{3}m$) at 2370°C. Cubic ZrO_2 is stable above 1700°C that induce large grain sizes of ZrO_2 around 50-70 μm . When cubic ZrO_2 is cooled down, phase transition occurs, and tetragonal precipitates are found in cubic matrix. The mixture of cubic and tetragonal phases affect the strength of materials due to the closure of cracks by expansion of the precipitates. The cubic-to-monoclinic and tetragonal phase transition is diffusionless and coexists a volume expansion of about 7% [49]. Since cubic and tetragonal modifications are unstable at low temperatures, a stabilizer for both phases are required. Most common stabilizer for cubic phase is

yttrium oxide (Y_2O_3) which is called Ytria-stabilized zirconia (YSZ) [50] and yttrium stabilized cubic can improve the strength and toughness of materials [51]. Tetragonal phase can be stabilized by sintered body of partially stabilized zirconia (PSZ) which contain low concentrations of yttria. Tetragonal phase with PSZ is stronger and tougher [52].

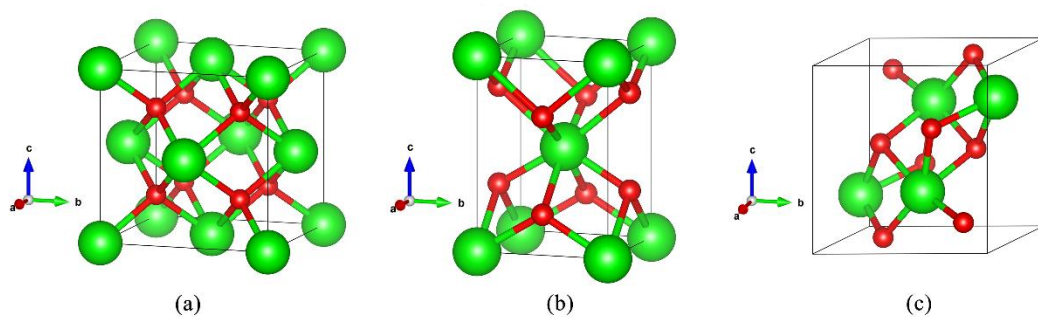


Figure 1.1 Unit cell of (a) cubic ZrO_2 (c- ZrO_2), (b) tetragonal ZrO_2 (t- ZrO_2), and (c) monoclinic ZrO_2 (m- ZrO_2). Zr and O are shown as green and red spheres respectively.

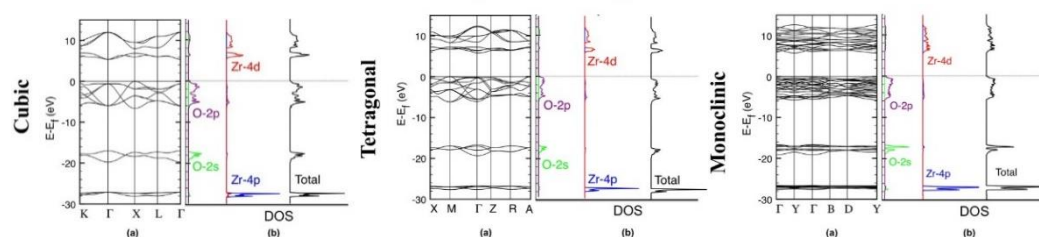


Figure 1.2 Calculated PBE0/Zr^{ECP}-O^{ECP} a) band structure and b) total and Zr-4d, Zr-4p, O-2s, O-2p projected DOS of I) cubic, II) tetragonal, and III) monoclinic ZrO_2 . The Fermi level has been set as origin of the energy scale. DOS for the cubic and tetragonal phases are multiplied by a factor of five and two, respectively [53].

Table 1.2 Physical Properties of Zirconia [49]

Property	Values
Polymorphism	
Monoclinic → tetragonal	1273-1473 (K)
Tetragonal → cubic	2643 (K)
Cubic → liquid	2953 (K)
Crystallography	
Monoclinic	
<i>a</i>	5.1454 Å
<i>b</i>	5.2075 Å
<i>c</i>	5.3107 Å
β	99°14'
Space group	$P2_1/c$
Tetragonal	
<i>a</i>	3.64 Å
<i>c</i>	5.27 Å
Space group	$P4_2/nmc$
Cubic	
<i>a</i>	5.065 Å
Space group	$Fm\bar{3}m$
Density	
Monoclinic	5.68
Tetragonal	5.86
Cubic	6.29
Thermal expansion coefficient ($10^{-6}/K$)	
Monoclinic	7
Tetragonal	12
Heat of formation (kJ/mol)	-1096.73
Boiling point (K)	4549
Thermal conductivity (W/m/K)	
at 100°C	1.675
at 1300 °C	2.094
Refractive index	2.15

The metastable cubic ZrO₂ can be synthesized by decomposition of Zr(OH)₄ which be prepared by the reaction in equation (1.1).



After preparation of Zr(OH)₄, the dehydration of Zr(OH)₄ at 110–285°C were obtained. The metastable cubic phase is present at 285°C as determined by X-ray diffraction. XRD pattern of the metastable cubic phase showed that unit cell dimension is 5.09 Å. The highest integrated relative intensity from (111) plane in cubic ZrO₂ suggested that this plane contains maximum numbers of Zr and O atoms [54]. The theoretical results show that (111) plane of cubic ZrO₂ is the most stable, in agreement with experimental data [53].

The theoretical studies of tetragonal ZrO₂ have been carried out. The structures of tetragonal phase of ZrO₂ were studied by using a periodic *ab initio* Hartree-Fock method with effective core potentials (ECP) basis sets for oxygen and zirconium atoms. The calculated unit cell dimensions of tetragonal phase are a=3.558 Å and c= 5.258 Å which agree with experimental data [55]. The experimental studies with surface of tetragonal phase were obtained. Tetragonal ZrO₂ were prepared via sol-gel method using high-purity reagents stabilized with Y₂O₃. The results from CO adsorption at 300 and ~ 78 K implied that the most energetic sites are selectively eliminated, but new families of less and less energetic sites are produced [56]. The theoretical study showed that (101) surface is the most stable surface for tetragonal phase [53].

The structure of monoclinic ZrO₂ was studied with X-ray techniques. The structure of monoclinic ZrO₂ was determined and refined by using Patterson and Fourier projections on the three faces of unit cell. The unit cell dimensions of monoclinic phase are a = 5.169 Å, b = 5.232 Å, c = 5.314 Å, and β = 99.0 Å. There are four ZrO₂ in the unit cell of monoclinic phase [57]. The experimental study of monoclinic surface was obtained. Monoclinic ZrO₂ was prepared by hydrolysis of Zr isopropoxide and calcination of amorphous hydroxide in air. Monoclinic ZrO₂ crystal structure shows a moderately regular termination, mostly along the (111) plane [58].

Nevertheless, the theoretical studies showed that $(\bar{1}11)$ is the most stable plane for monoclinic ZrO_2 [53]. The theoretical and experimental results are inconsistent. Despite the inconsistent results, the theoretical study using plane wave periodic DFT/PW91 calculations jointly with statistical thermodynamics describe that the ability of water adsorption on $(\bar{1}11)$ and (111) plane is closely. Water adsorption on $(\bar{1}11)$ and (111) plane exhibit full coverage of water in a similar bimodal way ($1 \rightarrow 2$ and $2 \rightarrow 2$, respectively) [59]. Therefore, the m- ZrO_2 (111) surface was selected to study in this work to compare with the similar plane of cubic ZrO_2 .

1.3 Literature reviews

Nowadays, ZrO_2 has been extensively used in many fields, such as industries or energy storage. A few experimental and theoretical studies of ZrO_2 surfaces, the chemical properties of the various ZrO_2 surfaces, and hydrogen gas or small gases storage on ZrO_2 were investigated.

In 2001, Pokrovski et al. [60] investigated the adsorption of CO and CO_2 on tetragonal (t- ZrO_2) and monoclinic ZrO_2 (m- ZrO_2) using infrared spectroscopy and temperature-programmed desorption spectroscopy. The results showed that the CO_2 adsorption capacity on m- ZrO_2 is more than the adsorption capacity on t- ZrO_2 . The CO adsorption capacity of m- ZrO_2 is more than that of t- ZrO_2 . The higher CO_2 adsorption capacity of m- ZrO_2 indicate the stronger Lewis basicity of O^{2-} anions and stronger Lewis acidity of Zr^{4+} cations on the surface of m- ZrO_2 is more than on the surfaces of t- ZrO_2 . Likewise the greater CO adsorption capacity of m- ZrO_2 is ascribed to the higher Lewis acidity and basicity of m- ZrO_2 compared with t- ZrO_2 .

In 2014, Kogler et al. [61] studied surface reactivity of ZrO_2 polycrystalline powder with H_2 by a pool of complementary experimental techniques, comprising volumetric methods (temperature-programmed volumetric adsorption/oxidation and thermal desorption spectrometry), spectroscopic techniques (in situ electric impedance and in situ FT-IR spectroscopy), and structural characterization methods (XRD and SEM). The volumetric hydrogen uptake during temperature-programmed reduction (TPR) suggested that the corresponding hydrogen uptake traces with the zeolite trap installed

and comprises two steps of hydrogen uptake at 500 and 800 K for ZrO_2 are observed. The results showed that ZrO_2 polycrystalline with monoclinic structure readily react with H_2 at lower temperatures. However, the H_2 uptake was lower than others easy-reducible oxides such as In_2O_3 . The ability of ZrO_2 to bind H_2 molecularly was restricted to nearby regions in the strongly reduced and dehydroxylated.

In 2014, Yang et al. [62] investigated the electronic structure properties of cubic- ZrO_2 (c- ZrO_2) by hybrid density functional theory which have applied the PBE, HSE03, HSE06, PBE0 basis sets in the calculations. From the calculations, the PBE0 was the appropriate basis set for electronic structure properties of c- ZrO_2 calculation. In this study, the c- ZrO_2 (111)-O and (110) surfaces that were the most stable surfaces and showed good insulating properties. The (110) and (111)-O surfaces were stoichiometric and there were no surface states within the energy gap. Their optical band gaps for the surfaces of c- ZrO_2 were considerably reduced in comparison to the c- ZrO_2 bulk. The narrow band gap of c- ZrO_2 surfaces made it possible to apply in photocatalyst or optical devices.

In 2015, The dispersion of small amounts of Ce^{4+} ions within bulk ZrO_2 have been synthesized in three methods by Gionco et al. [63]. Ce doped ZrO_2 materials have been synthesized via sol-gel synthesis and hydrothermal process using different precursors and different synthetic procedure for preparation Ce^{4+} inclusion. The Ce doped ZrO_2 show charge separation that induced in the solid by photons having energy much lower than that of the ZrO_2 band gap. The photoactivity of Ce doped ZrO_2 has been monitored using Electron Paramagnetic Resonance (EPR) spectroscopy and showed charge separation having $\lambda > 420$ nm. Therefore, lanthanide-doped Zirconium dioxide can be synthesized and affect to its band gap.

In 2016, Sinhamahapatra et al. [64] studied solar light absorption properties of oxygen-deficient black ZrO_2 . Since ZrO_2 is semiconductor with wide bandgap and can absorb ultraviolet light only, it is not recommended for sunlight absorption materials. The black ZrO_{2-x} was synthesized by controlled magnesiothermic reduction of monoclinic white ZrO_2 in 5% H_2/Ar and the excess Mg in ZrO_2 was removed by HCl washing, yielding the pure black films of monoclinic ZrO_2 . Raman spectroscopy revealed that the surface of black ZrO_2 has a number of huge oxygen vacancies during reduction. The oxygen vacancies affect to the disordered of surface. Electron

paramagnetic resonance (EPR) techniques is used to confirm the formation of huge oxygen vacancy and the reduction to Zr species in black ZrO₂. Black ZrO₂ absorb light in range of VIS and IR region dramatic enhance compared with white ZrO₂ which can only absorb UV light. Band gap of black ZrO₂ is 1.52 eV which decrease from white ZrO₂. The synthetic process of black ZrO₂ via magnesiothermic reduction in presence H₂/Ar affects to the efficiency of solar light absorption.

In 2016, the oxygen vacancy stabilized cubic ZrO₂ phase was experimentally and theoretically studied by Raza et al. [65]. In this study combined cold plasma-reactive magnetron sputtering with density functional theory (DFT) calculations. The experimental section used dc reactive magnetron sputtering (dc-RMS) to collect oxygen vacancies in ZrO₂ film. The crystallinity of ZrO₂ film was characterized by grazing incidence X-ray diffraction (GIXRD) and the result showed the peak positions matched reasonably to the cubic phase. The experimental result showed that integrating oxygen vacancies is single mechanism responsible of promoting ZrO₂ to the high-temperature cubic phase. The DFT result agree with experimental result that oxygen vacancies doped ZrO₂ film is cubic phase. Nevertheless, the experimental result exhibits that the ZrO₂ films change to monoclinic phase when deposited in the oxidize mode.

In 2016, Köck et al. [66] studied the adsorption and conduction behavior of H₂O and D₂O on yttria-stabilized zirconia (YSZ) with 8 mol% of Y₂O₃, Y₂O₃, and monoclinic ZrO₂ by using a combination of operando FT-IR spectroscopy, operando electrochemical-impedance spectroscopy, and dynamic moisture-sorption measurements. FT-IR spectroscopy indicated the H₂O adsorption ability of various surfaces as follow: Y₂O₃ > YSZ > monoclinic ZrO₂. The lowest water adsorption capacity of monoclinic ZrO₂ is due to the less hydroxylated than YSZ and Y₂O₃. Therefore, molecular water layers on monoclinic ZrO₂ exhibit no measurable protonic conduction.

In 2017, Ruiz Puigdollers et al. [67] investigated reduction of zirconia by water desorption from a hydrogenated surface using density functional theory (DFT) calculations with the PBE+*U* exchange-correlation functional and including dispersion forces on the adsorption, dissociation, diffusion of hydrogen on t-ZrO₂(101) surface. H₂ molecule is physisorbed with adsorption energies of -0.11 eV. The hydrogenated t-ZrO₂(101) surface was obtained by investigated adsorption and dissociation of a H₂

molecule on t-ZrO₂(101) surface. H₂ molecule are dissociated through a heterolytic mechanism into H⁺ and H⁻ ions. The energies of exothermic process of H₂ dissociation are -0.06 eV and Gibbs free energy for this process is endergonic with +0.34 eV. The reduction process of t-ZrO₂(101) surface is unfavorable due to the low reducibility. The hydrogenation reaction on t-ZrO₂(101) surface is possible to performed at below 70 K. This study exhibits the role of the tetragonal ZrO₂ surface on chemical and reducibility of oxide.

1.4 Objectives

In this work, the c-ZrO₂(111), t-ZrO₂(101), m-ZrO₂(111), their oxygen vacancy defective surfaces and lanthanide-doped c-ZrO₂(111) surfaces have been studied in terms of geometrical stability and electric conductivity and resistivity. Adsorption of hydrogen molecules on the c-ZrO₂(111), t-ZrO₂(101), m-ZrO₂(111), their oxygen vacancy defective surfaces and lanthanide-doped c-ZrO₂(111) surfaces have been investigated. The charge-transfer processes due to H₂ adsorption of the c-ZrO₂(111), t-ZrO₂(101), m-ZrO₂(111), their oxygen vacancy defective surfaces and lanthanide-doped c-ZrO₂(111) surfaces have been analyzed for prediction of their adsorption strength. Adsorption strengths of all surfaces in this work correlated with their H₂ adsorption energies have been investigated. The utilities of all studied surfaces for H₂ sensing materials have been suggested.

CHAPTER II

THEORETICAL BACKGROUND

Quantum chemistry applies quantum mechanics to investigate physicochemical properties of substances. Quantum mechanics includes three main methods, namely, *ab initio*, semi-empirical and the density-functional methods. These methods based on quantum mechanical principles, applying to study various chemical systems. Quantum chemical calculation can calculate for ground state of individual atom and molecule, transition state and excitation state that occur throughout the chemical reaction.

2.1 *Ab Initio* method

Ab initio calculations are computational method based on quantum chemistry solving Schrödinger equation,

$$H\psi = E\psi \quad (2.1)$$

where \hat{H} is Hamiltonian operator, E is the total energy of the system and ψ is the n -electron wave function. The kinetic and potential energies for each of the particles were indicated by Hamiltonian operator (\hat{H}) which are explained in equation (2.2).

$$H = -\frac{\hbar^2}{2m_e} \sum_i^{\text{electrons}} \nabla_i^2 - \frac{\hbar^2}{2} \sum_A^{\text{nuclei}} \frac{1}{M_A} \nabla_A^2 - \frac{e^2}{4\pi\epsilon_0} \sum_i^{\text{electrons}} \sum_A^{\text{nuclei}} \frac{Z_A}{r_{iA}} + \frac{e^2}{4\pi\epsilon_0} \sum_{i>}^{\text{electrons}} \sum_j^{\text{electrons}} \frac{1}{r_{ij}} + \frac{e^2}{4\pi\epsilon_0} \sum_{A>}^{\text{nuclei}} \sum_B^{\text{nuclei}} \frac{Z_A Z_B}{R_{AB}} \quad (2.2)$$

where Z is the nuclear charge, m_e is the mass of electron, R_{AB} is distance between nuclei A and B, r_{ij} is distance between electrons i and j , r_{iA} is distance between electrons i and nucleus A and ϵ_0 is the permittivity of vacuum [68].

Because the solution for many-electron system is absent, the Hartree-Fock method (HF) is the starting point of *ab initio* method. The Hartree-Fock method is the simplest approach of *ab initio* method that the instantaneous coulombic electron-electron repulsion is not specially considered. Only its average effect is included in this calculation.

In many-electron system, linear combination of atomic orbitals (LCAO) which all atomic orbitals are combined is applied to represent ψ . The possible approximate polyelectronic wavefunction as product of one-electron wavefunctions is written in equation (2.3).

$$\psi_0 = \psi_0(1)\psi_0(2)\psi_0(3)\dots\psi_0(n) \quad (2.3)$$

The function ψ_0 relies on the coordinates of all electrons in atom, $\psi_0(n)$ is a function of the n electron in atom which can be expanded by basis set. Because the HF nonlinearities approximation, the Self-consistent-field-procedure (SCF) is method that is used to solve the HF equation. The SCF cycles are continuously calculated until self-consistency is achieved. The spin orbitals and configuration state functions can be constructed by HF equation. Electrons in the system can move independently in a mean field potential because the Hartree-Fock method ignores electron correlation in the system. It is hard to perform the accurate calculations with large basis sets containing many atoms and electrons. Additionally, wavefunction cannot measure observable feature of molecule or atom. Therefore, the density functional theory (DFT) method becomes popular method to calculate in chemical system simulation [69].

2.2 Density functional theory (DFT) method

Density functional theory (DFT) method is based on the electron probability density function, simply called the electron density or charge density, and designated by $\rho(x, y, z)$ which is related to the “component” one-electron spatial wavefunctions Ψ_i (the molecular orbitals) of a single-determinant wavefunction Ψ by equation (2.4) [70].

$$\rho = \sum_{i=1}^n n_i |\Psi_i|^2 \quad (2.4)$$

2.2.1 The Kohn-Sham equations

From the wavefunction theory, the Hartree-Fock variational approach led to the Hartree-Fock equations which are used to calculate energy and the wavefunction. However, the Kohn-Sham equations which are the basis of current molecular DFT calculations have variational approach that might yield a way to calculate the energy and electron density. There are two ideas in Kohn-Sham method consist of (1) to express the molecular energy as a sum of terms, only one of which, a relatively small term. As a result, even moderately large errors in this term will not introduce large errors into the total energy. And (2) to use an initial guess of the electron density ρ in the Kohn-Sham equations to calculate an initial guess of the Kohn-Sham orbitals and energy levels. Then, this initial guess used to iteratively refine these orbitals and energy levels. The final Kohn-Sham orbitals are used to calculate electron density that can be used to calculate the energy of molecule. The electron density distribution of the reference system, which is by order the same as that of the ground state of our real system is given by

$$\rho_0 = \rho_r = \sum_{i=1}^{2n} |\psi_i^{KS}(1)|^2 \quad (2.5)$$

where the ψ_i^{KS} are the Kohn-Sham spatial orbitals. Substituting the above expression for the electron density in term of orbitals into the energy and varying E_0 relating to the ψ_i^{KS} which leads to the Kohn-Sham equation

$$\left[-\frac{1}{2} \nabla_i^2 - \sum_{\text{nuclei } A} \frac{Z_A}{r_{1A}} + \int \frac{\rho(\mathbf{r}_2)}{r_{12}} d\mathbf{r}_2 + v_{XC}(1) \right] \psi_i^{KS}(1) = \varepsilon_i^{KS} \psi_i^{KS}(1) \quad (2.6)$$

where ε_i^{KS} is the Kohn-Sham energy level and $v_{xc}(1)$ is the exchange correlation potential. The expression in bracket is the Kohn-Sham operator, \hat{h}^{KS} . Because the Kohn-Sham equations are a set of one-electron equation with the subscript i running from 1 to $2n$, over all the electrons in the system, they random installed electron number one in the Kohn-Sham orbitals and the exchange correlation potential. The exchange correlation potential v_{xc} obtained from the exchange-correlation energy E_{xc} which is a functional of $\rho(\mathbf{r})$ and the process to obtain v_{xc} is described as

$$v_{xc}(\mathbf{r}) = \frac{\delta E_{xc}[\rho(\mathbf{r})]}{\delta \rho(\mathbf{r})} \quad (2.7)$$

The differentiation of exchange correlation potential v_{xc} is shown as being with respect to $\rho(\mathbf{r})$, but $\rho(\mathbf{r})$ is explained in terms of Kohn-Sham orbitals. The Kohn-Sham equation can be defined by

$$\hat{h}^{KS}(1)\psi_i^{KS}(1) = \varepsilon_i^{KS}\psi_i^{KS}(1) \quad (2.8)$$

In Kohn-Sham system, the energy also compensates for self-repulsion in charge cloud of ρ . and for the deviation of the kinetic energy of noninteracting Kohn-Sham electrons from that of real electrons. For this reason, we should have the good functional handles that not only exchange correlation errors, but also self-repulsion and kinetic errors. The hybrid functional is the choice to improve calculations [70].

2.2.2 The functionals E_x and E_c

The functionals E_{xc} represent to the sum of an exchange-energy functional E_x and correlation-energy functional E_c which can be written as shown in equation (2.9).

$$E_{xc} = E_x + E_c \quad (2.9)$$

E_x for close-shell molecule can explain with this equation

$$E_x = -\frac{1}{4} \sum_{i=1}^n \sum_{j=1}^n \langle \theta_i^{\text{KS}}(1) \theta_j^{\text{KS}}(2) | 1/r_{12} | \theta_j^{\text{KS}}(1) \theta_i^{\text{KS}}(2) \rangle \quad (2.10)$$

where the factor of $\frac{1}{4}$ comes from the summing over the electrons, which gives four times as many terms in double sum in this equation. The DFT exchange energy is close to the Hartree-Fock exchange energy because KS orbitals are found to resemble rather closely Hartree-Fock orbitals. E_c is defined by the difference between E_x and E_{xc} which can avoid the poor results from evaluation of E_c because of cancellation of error and giving better results. E_x and E_c are negative values, with $|E_x|$ being much larger than $|E_c|$ [69].

2.2.3 Generalized-gradient (GGA) Functionals

The generalized-gradient approximation (GGA) which also used in term gradient-corrected functionals is the functions that correct the local-spin-density approximation (LSDA) for the variation of electron density with position by including the gradients of ρ^α and ρ^β in the integrand of LSDA. Therefore

$$E_{xc}^{\text{GGA}}[\rho^\alpha, \rho^\beta] = \int f(\rho^\alpha(\mathbf{r}), \rho^\beta(\mathbf{r}), \nabla\rho^\alpha(\mathbf{r}), \nabla\rho^\beta(\mathbf{r})) d\mathbf{r} \quad (2.11)$$

where f is some function of the spin densities and their gradients. GGA represent to generalized-gradient approximation. Gradient-corrected functionals are relate the values of ρ at \mathbf{r} and in an infinitesimal neighborhood of \mathbf{r} . E_{xc}^{GGA} can be split into exchange and correlation parts, in form

$$E_{xc}^{\text{GGA}} = E_x^{\text{GGA}} + E_c^{\text{GGA}} \quad (2.12)$$

Approximate gradient-corrected exchange and correlation energy functionals are developed via theoretical considerations which is the known behavior of true

functionals E_x and E_c in disparate limiting situations as a guide. The selection values of parameters in the functionals can give good performance to know values of numerous molecular properties. In this work uses the Perdew-Burke-Ernzerhof (PBE) exchange and correlation functional which has no empirical parameters. The PBE functional is not only used in periodic fields but also broadly use in solids calculation employing with DFT [69].

2.3 Basis sets

Basis sets are collection of mathematical functions, linear combinations of which yield molecular orbitals that used to solve the Schrödinger equation. The functions are usually, but not regularly, centered on atomic nuclei. Basis functions usually explain the electron distribution around an atom and combining atomic basis functions yields the electron distribution in molecule as whole. Basis functions which are not center on atoms can be considered to be on ghost atoms. There are many types of basis sets that should select the appropriate basis set to atom to obtain the best result [71].

2.3.1 Gaussian basis set

Basis sets that made up of a finite number of well-defined functions centered of each atom are required in the linear combination of atomic orbitals (LCAO) approximation. Those functions would be corresponding closely to the exact solution of hydrogen atom. Nevertheless, the use of these functions was not cost effective, and early numerical calculations were implemented using nodeless Slater-type orbitals (STOs) which defined by

$$\phi(r, \theta, \phi) = \frac{(2\zeta / a_0)^{n+1/2}}{[(2n)!]^{1/2}} r^{n-1} e^{-\zeta r/a_0} Y_l^m(\theta, \phi) \beta \quad (2.13)$$

Here, n , m , and l denote the usual quantum number and ζ is the effective nuclear charge. The Slater functions was popular in the years immediately but soon deserted because they lead to integrals that are difficult if not impossible to evaluate analytically.

The cost of calculations can be reduced if the AOs are expanded in terms of Gaussian functions which are in form

$$g_{ijk}(r) = Nx^i y^j z^k e^{-\alpha r^2} \quad (2.14)$$

In this equation, x , y , and z are the position coordinates measured from the nucleus of an atom; i , j , and k are non-negative integers that the sum of these values determines the types of orbitals, and α is an orbital exponent. Gaussian functions lead to integrals that are easily evaluated. Except for semi-empirical models, which do not actually entail evaluation of large number of difficult integrals, all practical quantum chemical models now make use of Gaussian functions.

The different radial dependence of STOs and Gaussian function, first, the Gaussian functions are appropriate choices for AOs. The solution to this problem is to approximate the STO by a linear combination of Gaussian function having different α values, rather than by a single Gaussian function. Using more Gaussian functions can improve cloud electrons to fit well in AOs.

In practice, instead of taking individual Gaussian functions as members of basis set, a normalized linear combination of Gaussian functions with fixed coefficients gives the value that is optimized either by searching minimum atom energies or by comparing calculated and experimental results for representative molecule. These linear combinations are called contracted functions that become the elements of the basis set. The coefficients are variable [68].

2.3.2 Minimal Basis set

The minimal basis sets have one and only one basis function defined for each type of orbital core through valence. There are two types of minimal basis sets which are Slater type orbitals (STO) and Gaussian type orbital (GTO). The most widely used and extensively documented is the STO-3G basis set. Each of the basis functions is expanded in terms of three Gaussian functions, where the values of the Gaussian exponents and the linear coefficients have been determined by least squares as best fits to Slater-type (exponential) functions. There are two obvious deficiencies in the minimal basis sets: the first is that basis sets can be described atom with spherical

molecular environments or nearly spherical molecular environments better than atoms with aspherical environments. So, this basis set will be biased in favor of those incorporating the most spherical atoms. The second deficiency is that basis functions are atom centered. As a result, this basis cannot describe electron distribution between nuclei, which are a critical element of chemical bond [68].

2.3.3 Split-Valence Basis sets

The split-valence basis set correspond to core atomic orbitals by one set of functions and valence atomic orbitals by two sets of functions, $1s$, $2s^i$, $2p_x^i$, $2p_y^i$, $2p_z^i$, $2s^o$, $2p_x^o$, $2p_y^o$, $2p_z^o$ for lithium to neon and $1s$, $2s$, $2p_x$, $2p_y$, $2p_z$, $3s^i$, $3p_x^i$, $3p_y^i$, $3p_z^i$, $3s^o$, $3p_x^o$, $3p_y^o$, $3p_z^o$ for sodium to argon. Note that the valence $2s$ ($3s$) functions are also split into inner, i and outer, o components, and that hydrogen atoms are also represented by inner and outer valence ($1s$) functions. There are many types of split-valence basis sets, but the simplest basis sets are 3-21G and 6-31G [68].

2.3.4 Polarization Basis sets

The second deficiency of a minimal basis sets that basis functions are centered on atom rather than between atoms can be improve by the inclusion of polarization functions. The inclusion of polarization functions can be thought about either in term of hybrid orbitals. The term arises from the fact that d functions permit the electron distribution to be polarized (displaced along a particular direction). Polarization functions enable the SCF process to establish a more anisotropic electron distribution than would otherwise be possible. The simplest polarization basis set is 6-31G* which formed from 6-31G by adding a set of d -type polarization functions written in term of a single Gaussian for each heavy atom. Polarization functions have chosen Gaussian exponents to give the lowest energies for representative molecules. However, the polarization basis function does not stand for initial atomic orbital (IAO) which is useful to analyses obtained atomic orbitals and molecular orbitals because, the basis function of p orbital is combined to s orbital, and the basis function of d orbital is combined to p orbital in many cases [68].

2.3.5 Diffuse Basis sets

The highest energy electrons for molecules in calculations involving anions such as absolute acidity calculations and calculations of molecules in excited states may only be associated with specific atoms (or pairs of atoms) loosely. Because, in highest spin state, electrons are assigned in more outer shell orbital where electron is unoccupied in lowest spin state. The diffuse basis functions can supplement for increase accuracy in specific calculations. For example, diffuse *s*- and *p*-type functions, on heavy (non-hydrogen) atoms (designated with a plus sign as in 6-31+G* and 6-31+G**). It may also be desirable to provide hydrogens with diffuse *s*-type functions (designated by two plus signs as in 6-31++G* and 6-31++G**) [68].

2.3.6 Effective Core Potentials (Pseudopotentials)

The heavy elements which have many of electrons in periodic table require to use many basis functions to describe them. In heavy elements, the extra electrons are mostly core electron which can be enough a minimal representation. Effective core potentials (ECP) are functions that represent the combined nuclear–electronic core to the remaining electrons. ECP is a nuclear point charge reduced in magnitude by the number of core electrons. ECPs are greatly more complex in the *ab initio* theory. ECPs appropriately describe not only Coulomb repulsion effects, but also adherence to the Pauli principle. ECP describes the behavior of an atomic core, relativistic effects can be canceled, thus removed from the problem of finding proper wavefunctions for the remaining electrons, because the core electrons in very heavy elements reach velocities adequately near the speed of light that show relativistic effect which a non-relativistic Hamiltonian operator is unable of accounting for such effects. A non-relativistic Hamiltonian operator can be significant for chemical properties. The construction of ECP is about the number of electrons to include in the core. Large-core ECPs include everything but the valence shell, whereas small-core ECPs scale back to the next lower shell. It is valuable to explicitly include next lower shell of electron in the calculations because polarization of the sub-valence shell can be chemically importance in heavier metals. Popular ECPs include those of Hay and Wadt which is used in this study. The

Hay–Wadt ECPs are non-relativistic for the first row of transition metals because relativistic effects are usually quite small for them [70].

2.4 Mülliken population analysis

Mülliken population analysis is method to calculated partial charges of molecule. The concept of this method is the electrons being divided up amongst the atoms according to the degree to which different atomic AO basis function contribute to the overall wavefunction. The equation expresses the total number of electrons are shown in equation (2.15), and expanding the wavefunction in its AO basis set

$$\begin{aligned}
 N &= \sum_j^{\text{electrons}} \int \psi_j(\mathbf{r}_j) \psi_j(\mathbf{r}_j) d\mathbf{r}_j \\
 &= \sum_j^{\text{electrons}} \sum_{r,s} \int c_{jr} \varphi_r(\mathbf{r}_j) c_{js} \varphi_s(\mathbf{r}_j) d\mathbf{r}_j \\
 &= \sum_j^{\text{electrons}} \left(\sum_r c_{jr}^2 + \sum_{r \neq s} c_{jr} c_{js} S_{rs} \right)
 \end{aligned} \tag{2.15}$$

where r and s indicated to O basis function φ_r , c_{jr} is the coefficient of basis function r in MO j , and S is the usual overlap matrix element.

From the last line of equation (2.15), it can be concluded that electron associated with only a single basis function should be thought of belonging entirely to the atom on which that basis function resides. From the second term of last line in equation (2.15), Mülliken recommended that one might as well divide these up evenly between the two atoms on which basis functions r and s reside. From this prescription and moreover divide the basis functions up over atom k so as to calculate the atomic population N_k which describe in equation (2.16).

$$N_k = \sum_j^{\text{electrons}} \left(\sum_{r \in k} c_{jr}^2 + \sum_{r,s \in k, r \neq s} c_{jr} c_{js} S_{rs} + \sum_{r \in k, s \in k} c_{jr} c_{js} S_{rs} \right) \quad (2.16)$$

Note that the orthonormality of basis functions of the difference of angular momentum both residing on the same atom k as many terms in the second sum on Eq to be zero. The Mülliken partial atomic charge can be described by equation (2.17).

$$q_k = Z_k - N_k \quad (2.17)$$

where, Z is the nuclear charge and N_k is computed according to equation (2.16). Mülliken charges have disadvantage of their population analyses being orbital-based. However, the advantage of Mülliken charges is the great speed to computed the charges as can be recommended to use in qualitative analysis fields [70].

2.5 Band structure

When two atoms are engaged to form a chemical bond, their atomic orbitals overlap, giving rise to two frontier orbitals, viz., valence bonding orbital and anti-bonding orbital. From this concept, the large number of atoms in solid affect to the number of orbitals and closely spaced energy level is also large. This result is a band of orbitals of similar energy, rather than the discrete energy levels of small molecules. The electrons are contained in these bands. The highest of electrons containing in energy band names the valence band. The nearby valence band which is empty of electrons in this band names the conduction band.

The difference of energies between the highest valence band and the lowest conduction band which called band gap can be used as a criterion to classify type of materials. The large energy of band gap indicates the insulators. The electrons in insulator are restricted in their motion due to prevention motion of band gap. In case with partly filled orbitals, the gap between the valence and conduction bands is blurred. Electrons require little energy to move to higher energy levels within the band. Therefore, electron can move independently throughout the crystal, as are the holes in

the band. These materials are conductors. As a required of electrons occupying the lowest energy levels, the holes tend to be in the upper levels within the band. Electrons are being delocalized with these band which is corresponding with molecular orbital theory. Temperature can impact to bands. When temperature is raised up, more electrons are excited into upper band, more holes are found in lower band and conductance increase. These are the characteristics of semiconductors which have much higher conductivity than insulator and much lower conductivity than conductors. To describe the concentration of energy levels within bands, the density of states (DOS) is used [72].



CHAPTER III

COMPUTATIONAL DETAILS

3.1 Polymorphic Zirconium dioxide structures optimization

Optimized structures of the *c*-ZrO₂(111), *t*-ZrO₂(101) and *m*-ZrO₂(111) surfaces with respective space groups $Fm\bar{3}m$, $P4_2/nmc$, and $P2_1/c$, their hydrogen molecule adsorption, and the lanthanide-doped *c*-ZrO₂(111) surfaces have been deduced by periodic density functional theory (DFT) calculation method including London-type empirical correction for dispersion interactions [73], which is called the *D2 version of Grimme's* dispersion method. The empirical parameters of the *D2 method of Grimme* for the elements used in this work are shown in Appendices, Table A–1.

The PBE GGA functionals, Perdew-Becke-Ernzerhof (PBE) exchange and correlation [74], based on the expansion of the crystalline orbitals, have been performed with the CRYSTAL14 software package [75]. The basis sets HAYWSC–311d31G [76] and 8-411 [77] were employed for Zr and O atoms, respectively of ZrO₂ surfaces, which give well result in previous work [43, 78]. The basis sets 5-11G* [79] was employed for the H atom of hydrogen molecule gas. The effective core potentials (ECP) basis sets were used for lanthanide elements including Ce [80] and Eu dopants, which is appropriate for this calculation. All basis sets were taken from the CRYSTAL14 homepage. The spin-polarization was applied for all calculations as the oxygen-vacancy defective structure of ZrO₂ surfaces. The tolerances for geometry optimization convergence, truncation threshold of 10^{-8} , 10^{-8} , 10^{-8} , 10^{-8} , and 10^{-16} for the coulomb-exchange were selected, and Fock/Kohn-Sham matrices mixing was set to 80. The Monkhorst-Pack shrinking factor of $11 \times 11 \times 1$ *k*-point was used to sample the Brillouin zone.

The full optimized bulk lattice parameters of the *c*-ZrO₂, *t*-ZrO₂ and *m*-ZrO₂ crystals are respectively (*a*=5.120), (*a*=3.622, *c*=5.205), and (*a*=5.150, *b*=5.287, *c*=5.295, β =98.0) which are in good agreement with the x-ray crystallographic data [55, 81, 82], as shown in Table A–2.

The polymorphic ZrO surfaces were respectively generated by slabbing parallel (111), (101), (111) planes of full optimized structures of the bulk c-ZrO₂, t-ZrO₂, and m-ZrO₂, using SLABCUT keyword. All the structures of the polymorphic ZrO₂ surfaces consist of 48 ZrO₂ (Zr₄₈O₉₆) because there are different layers of various polymorphic ZrO₂ surfaces. The c-ZrO₂(111), t-ZrO₂(101), m-ZrO₂(111) slab surfaces of which *supercell sizes* are (4×4), (4×2), and (2×2), respectively. These supercell sizes were selected due to the appropriate size to represent their surface structure in calculations. The nine layers (6 O- and 3 Zr-layers) of the c-ZrO₂(111), 15 layers (12 O- and 3 Zr-layers) of the t-ZrO₂(101), and 30 layers (24 O- and 6 Zr-layers) of the m-ZrO₂(111), surfaces were modeled in the computations as shown in Figure A–1 in Appendices.

The structure of c-ZrO₂(111) surface is flat that constituted by the 3–fold coordinated oxygen O atoms (O_{3C}) and 7–fold coordinated Zr atoms (Zr_{7C}) as shown in Figure A–4(a), and the vertical levels of atomic layers of the surface are in order: O_{3C} > Zr_{7C}. The t-ZrO₂(101) is constituted by the 3–fold coordinated oxygen O atoms (O_{3C}) and 7–fold coordinated Zr atoms (Zr_{7C}) shown in Figure A–4(b), and its vertical levels of atomic layers of the surface are in order: O_{3C} > O_{3C} > Zr_{7C}. The m-ZrO₂(101) is constituted by the 6–fold coordinated Zr atoms (Zr_{6C}), 7–fold coordinated Zr atoms (Zr_{7C}), 2–fold coordinated oxygen O atoms (O_{2C}), and 3–fold coordinated oxygen O atoms (O_{3C}) as shown in Figure A–4(c) and its vertical levels of atomic layers of the surface are in order: O_{2C} > O_{3C} > O_{2C} > O_{3C} > Zr_{6C} > Zr_{7C}.

On the c-ZrO₂(111) and t-ZrO₂ surface, there are two coordinative types of Zr atoms, Zr_{7C} and Zr_{8C}, that are Zr³⁺ and Zr⁴⁺, respectively. For the m-ZrO₂(111) surface, there are two coordinative types of Zr atoms, namely Zr_{6C} and Zr_{7C}, respectively Zr³⁺ and Zr⁴⁺, were found.

The partial charges of atoms in molecules were obtained from the Mülliken population analysis as installed in the CRYSTAL14 software package. All calculation in this work were performed with CRYSTAL14 program and all the molecular images were plotted by using the VESTA 3.4.0 software [83].

3.2 Adsorption of hydrogen molecule on the polymorphic ZrO₂ surfaces

The adsorption energies of H₂ adsorbed on the pristine (ΔE_{ads}^{pris}) and oxygen vacancy defective ZrO₂ (ΔE_{ads}^{def}) surfaces are defined as shown in equations (3.1) and (3.2).

$$\Delta E_{ads}^{pris} = E_{H_2/ZrO_2} - (E_{H_2} + E_{ZrO_2}) \quad (3.1)$$

$$\Delta E_{ads}^{def} = E_{H_2/[ZrO_2+V_O]} - (E_{H_2} + E_{[ZrO_2+V_O]}) \quad (3.2)$$

where E_{H_2/ZrO_2} is the total energy of the H₂/ZrO₂. E_{H_2} and E_{ZrO_2} are the total energies of hydrogen gas and clean ZrO₂ surface, respectively. $E_{H_2/[ZrO_2+V_O]}$ and $E_{[ZrO_2+V_O]}$ are the total energies of the H₂/[ZrO₂ + V_O] and [ZrO₂ + V_O], respectively.

3.3 The electrical conductivity

Electrical conductivity (σ) is a function of the energy gap (E_g) [84], can expressed in equation (3.3) [85].

$$\sigma = \sigma_o T^{3/2} \exp\left(\frac{-E_g}{2k_B T}\right) \quad (3.3)$$

where σ_o is the constant. T and k_B are the absolute temperature and Boltzmann constant (8.6181×10^{-5} eV K⁻¹), respectively. As the energy gaps of the adsorption-state (E_g^{ads}) and clean surface (E_g^{clean}), the sensitivity of electrical conductivity (S_σ) of a system of H₂ adsorbed on individual surfaces is defined as shown in equation (3.4) [86].

$$S_\sigma\% = \left| \frac{\sigma_{ads} - \sigma_{clean}}{\sigma_{clean}} \right| \times 100 \quad (3.4)$$

where σ_{ads} and σ_{clean} are the electrical conductivities of the H₂ adsorbed ZrO₂ and clean ZrO₂ surfaces, respectively. As the same value of $\sigma_o T^{3/2}$ for the system of

individual ZrO₂ and their H₂ adsorptions was assumed, thus $S_{\sigma}^{\%}$ can be described in equation (3.5).

$$S_{\sigma}^{\%} = \left| \frac{\exp\left(\frac{-E_g(ads)}{2k_B T}\right) - \exp\left(\frac{-E_g(clean)}{2k_B T}\right)}{\exp\left(\frac{-E_g(clean)}{2k_B T}\right)} \right| \times 100 \quad (3.5)$$

The electrical resistivity (ρ) is a function of E_g as shown in equation (3.6).

$$\rho = \rho_o T^{-3/2} \exp\left(\frac{E_g}{2k_B T}\right) \quad (3.6)$$

where ρ_o is constant. The sensitivity of electrical resistivity ($S_{\rho}^{\%}$) of a system of H₂ adsorbed on individual ZrO₂ surfaces is defined as shown in equation (3.7).

$$S_{\rho}^{\%} = \left| \frac{\exp\left(\frac{E_g(ads)}{2k_B T}\right) - \exp\left(\frac{E_g(clean)}{2k_B T}\right)}{\exp\left(\frac{E_g(clean)}{2k_B T}\right)} \right| \times 100 \quad (3.7)$$

3.4 The bond strength

The bond strengths (BS in eV) of Zr bonding to H, in all the H₂/[ZrO₂ + V_O] complexes have been derived from Coulomb's law [87] as defined in equation (3.8) :

$$BS = \frac{k q_{Zr} q_H}{r_{Zr-H}} \times 6.241506363094 \times 10^{18} \quad (3.8)$$

where k is the Coulomb's constant ($8.9875517873681764 \times 10^9 \text{ Nm}^2/\text{C}^2$). q_{Zr} and q_H are electric charges (C) of Zr and H atoms, respectively and r_{Zr-H} (m) is the Zr-H bond length.

CHAPTER IV

RESULTS AND DISCUSSION

4.1 Surface structures and relative stabilities of polymorphic ZrO_2 surfaces

The optimized structures of the pristine c- ZrO_2 (111), t- ZrO_2 (101) and m- ZrO_2 (111) surfaces are shown in Figure 4.1. The optimized structures of (4x4) c- ZrO_2 (111), (4x2) t- ZrO_2 (101) and (2x2) m- ZrO_2 (111) surfaces are shown in Figure A-4. The selected geometrical parameters of the pristine polymorphic ZrO_2 surfaces are shown in Table A-3. The Zr-Zr bond lengths of the surfaces are in order: t- ZrO_2 (101) (3.622 Å) ~ c- ZrO_2 (111) (3.620 Å) > m- ZrO_2 (111) (3.453, 3.948 Å).

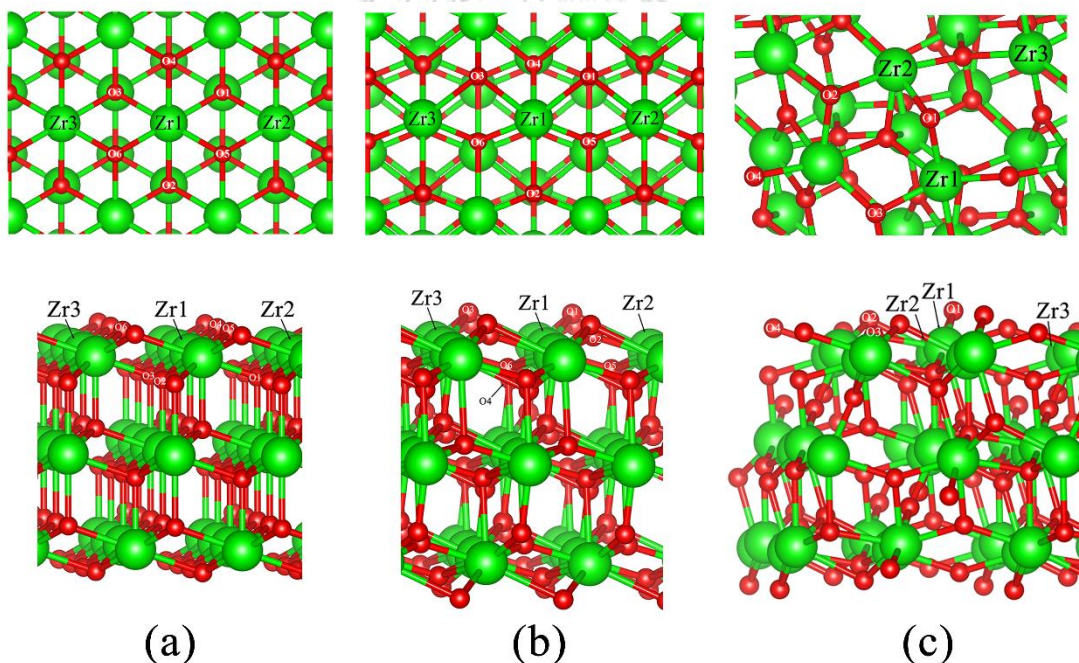


Figure 4.1 Structures of (a) c- ZrO_2 (111), (b) t- ZrO_2 (101), and (c) m- ZrO_2 (111) surfaces. The labeled atoms of these surfaces are shown. The top and bottom panels show the top and side views, respectively.

The optimized structures of the oxygen vacancy defective ZrO_2 surfaces, namely $[\text{c-ZrO}_2(111)+\text{V}_\text{o}]$, $[\text{t-ZrO}_2(101)+\text{V}_\text{o}]$, and $[\text{m-ZrO}_2(111)+\text{V}_\text{o}]$ are shown in Figure 4.2. The optimized structures of (4×4) $[\text{c-ZrO}_2(111)+\text{V}_\text{o}]$, (4×2) $[\text{t-ZrO}_2(101)+\text{V}_\text{o}]$ and (2×2) $[\text{m-ZrO}_2(111)+\text{V}_\text{o}]$ surfaces are shown in Figure A–5.

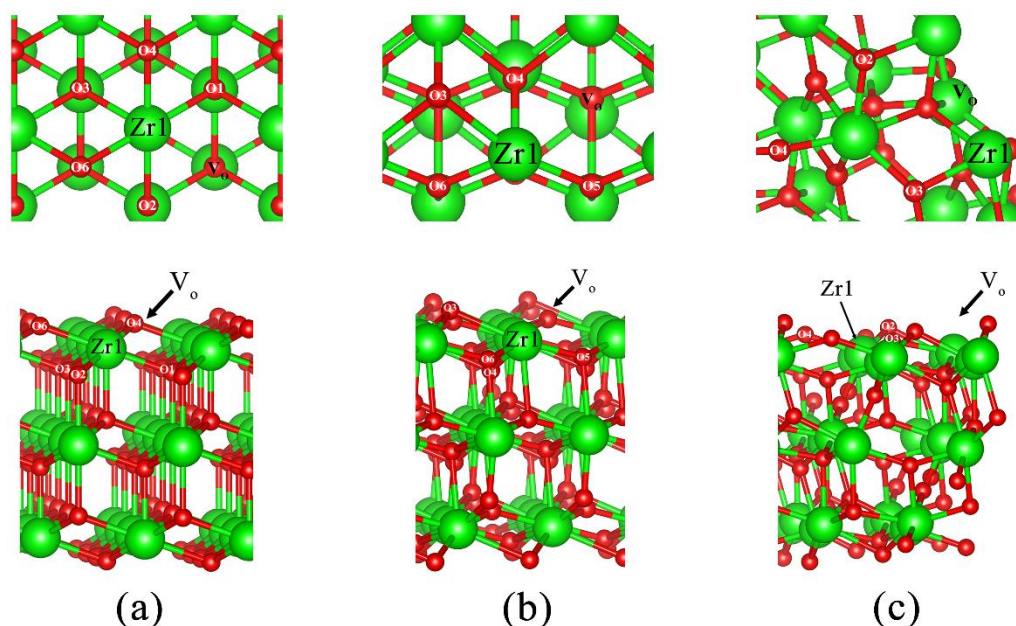


Figure 4.2 Structures of the (a) $[\text{c-ZrO}_2(111)+\text{V}_\text{o}]$, (b) $[\text{t-ZrO}_2(101)+\text{V}_\text{o}]$, and (c) $[\text{m-ZrO}_2(111)+\text{V}_\text{o}]$ surfaces. The labeled atoms of these surfaces are shown. The top and bottom panels show the top and side views, respectively. V_o indicates the oxygen vacancy.

The $\text{c-ZrO}_2(111)$, $\text{t-ZrO}_2(101)$, $\text{m-ZrO}_2(111)$ and their oxygen vacancy defective surfaces (see the modeling details in Section 3.1) consist of 48 ZrO_2 ($\text{Zr}_{48}\text{O}_{96}$), which are equivalent to (4×4) , (4×2) and (2×2) unit cells. Therefore, the relative stabilities of the pristine and oxygen vacancy defective surfaces are evaluated from the comparison of their total energies (Table 4.1). It shows that the relative stabilities of the pristine surfaces are in order: $\text{c-ZrO}_2(111)$ ($\Delta E_{\text{rel}} = 0.00 \text{ eV}$) $>$ $\text{t-ZrO}_2(101)$ ($\Delta E_{\text{rel}} = 12.75 \text{ eV}$) $>$ $\text{m-ZrO}_2(111)$ ($\Delta E_{\text{rel}} = 13.91 \text{ eV}$). And the relative stabilities of the oxygen vacancy defective surfaces are in order: $[\text{c-ZrO}_2(111)+\text{V}_\text{o}]$ ($\Delta E_{\text{rel}} = 0.00 \text{ eV}$) $>$ $[\text{t-ZrO}_2(101)+\text{V}_\text{o}]$ ($\Delta E_{\text{rel}} = 12.05 \text{ eV}$) $>$ $[\text{m-ZrO}_2(111)+\text{V}_\text{o}]$ ($\Delta E_{\text{rel}} = 12.82 \text{ eV}$). The $\text{c-ZrO}_2(111)$ surface is

the most stable surface for pristine and oxygen vacancy defective surface due to high symmetry of cubic structure.

Table 4.1 Total and relative energies of the c-ZrO₂(111), t-ZrO₂(101), and m-ZrO₂(111) surfaces and their oxygen vacancy defective surfaces.

Forms ^a	E_{total} ^b	ΔE_{rel} ^c
<i>Pristine:</i>		
c-ZrO ₂ (111)	-9467.52905449	0.00
t-ZrO ₂ (101)	-9467.06040569	12.75
m-ZrO ₂ (111)	-9467.01791227	13.91
<i>Oxygen vacancy defective:</i>		
[c-ZrO ₂ (111)+V _O]	-9392.13150240	0.00
[t-ZrO ₂ (101)+V _O]	-9391.68858706	12.05
[m-ZrO ₂ (111)+V _O]	-9391.66025170	12.82

^a The formulae of all the surface structures consist of 48 ZrO₂ units (Zr₄₈O₉₆), see Figure A-5.

^b In au. (1 Hartree = 27.2114 eV)

^c Compared with the most stable surface in eV.

4.2 Adsorption of a single hydrogen molecule on polymorphic ZrO₂ surfaces

The optimized surfaces of the structures of the c-ZrO₂(111), t-ZrO₂(101), and m-ZrO₂(111) surfaces are shown in Figure 4.1. All the adsorption structures of hydrogen molecules on the c-ZrO₂(111), t-ZrO₂(101), and m-ZrO₂(111) surfaces are shown in Figure 4.3. The adsorption structures of single hydrogen molecule adsorbed on the c-ZrO₂(111), t-ZrO₂(101), and m-ZrO₂(111) surfaces are denoted as H₂/c-ZrO₂(111), H₂/t-ZrO₂(101), and H₂/m-ZrO₂(111), respectively.

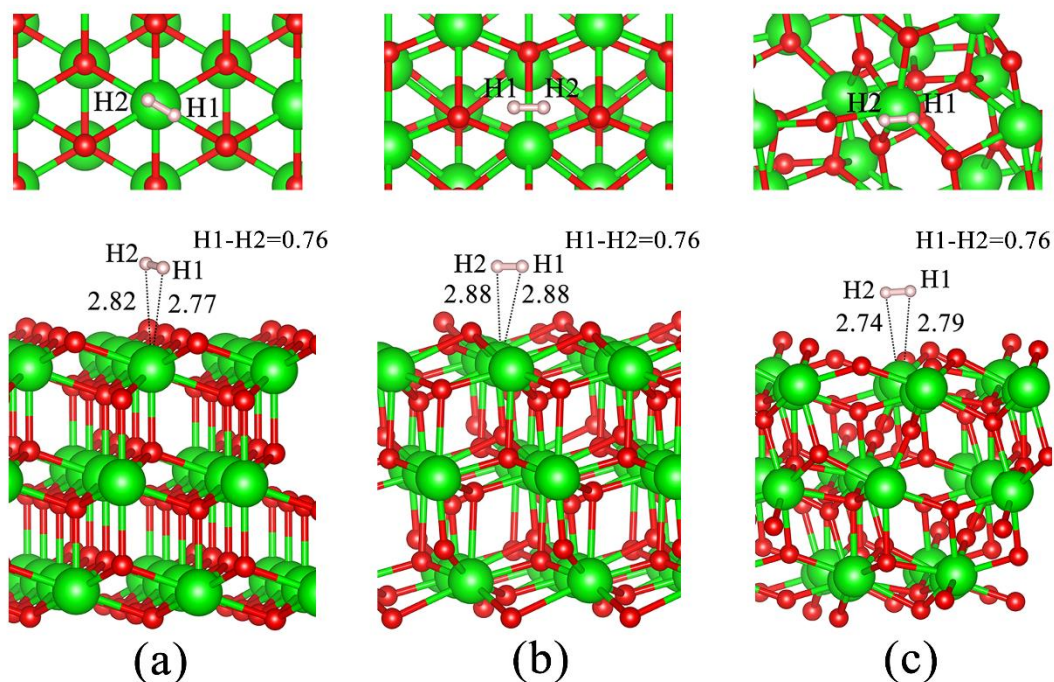


Figure 4.3 Optimized structures of hydrogen molecule adsorption on (a) c-ZrO₂(111), (b) t-ZrO₂(101), and (c) m-ZrO₂(111). The top and bottom panels show the top and side views, respectively. The bond lengths of H–H and separation distances between hydrogen molecule and ZrO₂ surface are in Å.

Adsorption structure of the H₂/c-ZrO₂(111) surface shows that the H₂ locates over the Zr atom as the adsorption site with parallel to the molecular (111) plane and the separation distances of [Zr···H1(H₂)] = 2.77 Å, [Zr···H2(H₂)] = 2.82 Å, were found. The adsorption structure of the H₂/t-ZrO₂(101), the H₂ situates over the Zr atom as the adsorption site with parallel to the molecular (101) plane which is consistent with previous work [88] and the separation distances of [Zr···H1(H₂)] = 2.88 Å, [Zr···H2(H₂)] = 2.88 Å, were found. Adsorption structure of the H₂/m-ZrO₂(111) shows that H₂ situates over the Zr atom as the adsorption site with almost parallel to the molecular (111) plane which is similar to the geometry of H₂ adsorbed on m-ZrO₂($\bar{1}11$) in previous work [89]. The separation distances of [Zr···H1(H₂)] = 2.79 Å, [Zr···H2(H₂)] = 2.74 Å of H₂ adsorption on m-ZrO₂(111) surface, were found.

The adsorption abilities of all the pristine ZrO₂ surfaces on H₂ are in order: c-ZrO₂(111) ($\Delta E_{\text{ads}} = -1.89$ eV) > m-ZrO₂(111) ($\Delta E_{\text{ads}} = -1.67$ eV) > t-ZrO₂(101) ($\Delta E_{\text{ads}} = -0.27$ eV), as shown in Table 4.2. Adsorption energies of H₂ molecule on

t-ZrO₂(101) surface are consistent with H₂ adsorption energies on t-ZrO₂(101) which equal to -0.31 eV surface in previous work [88]. H₂ adsorption on these pristine ZrO₂ surfaces are physisorption.

The optimized structures of the [c-ZrO₂(111)+V_O], [t-ZrO₂(101)+V_O], and [m-ZrO₂(111)+V_O] surfaces are shown in Figure 4.2. All the adsorption structures of hydrogen molecules on the [c-ZrO₂(111)+V_O], [t-ZrO₂(101)+V_O], and [m-ZrO₂(111)+V_O] are shown in Figure 4.4. The adsorption structures of a hydrogen molecule adsorbed on the [c-ZrO₂(111)+V_O], [t-ZrO₂(101)+V_O], and [m-ZrO₂(111)+V_O] surfaces, denoted as H₂/[c-ZrO₂(111)+V_O], H₂/[t-ZrO₂(101)+V_O], and H₂/[m-ZrO₂(111)+V_O] are all dissociative adsorptions as shown in Figure 4.4.

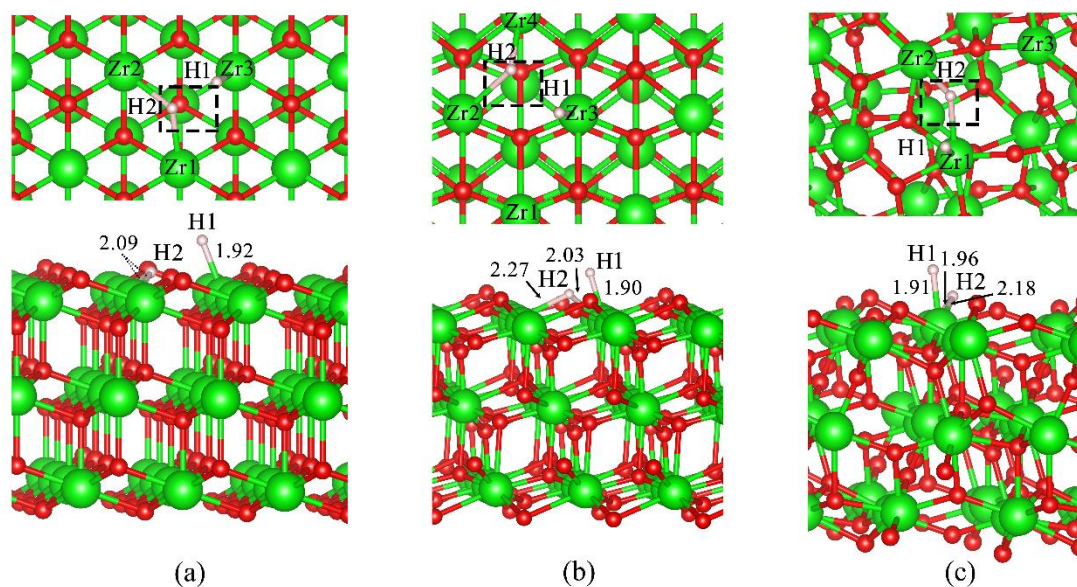


Figure 4.4 Optimized structures of hydrogen molecule dissociative adsorption on (a) [c-ZrO₂(111)+V_O], (b) [t-ZrO₂(101)+V_O], and (c) [m-ZrO₂(111)+V_O] surfaces. The top and bottom panels show the top and side views, respectively. The bond lengths of Zr–H are in Å. The rectangular areas (black dashed line) indicate oxygen vacancy position on surfaces.

The adsorption structure of the H₂/[c-ZrO₂(111)+V_O] is the dissociative H₂ adsorption of which one H atom was adsorbed on two Zr atoms (Zr1 and Zr2), and one H atom on the third Zr atom (Zr3), as shown in Figure 4.4(a) and the bond lengths of

$[Zr1-H1] = [Zr2-H1] = 2.09$, and $[Zr3-H2] = 1.92$ Å, were found. The separation distance $[H1 \cdots H2]$ of 1.93 Å was found. The H₂ dissociative adsorption structure of the H₂/t-ZrO₂(101), one H atom was adsorbed on two Zr atoms (Zr2 and Zr4) and one on the third Zr atom (Zr3), as shown in Figure 4.4(b) and the bond distances of $[Zr2-H2] = 2.27$, $[Zr4-H2] = 2.03$, and $[Zr3-H1] = 1.90$ Å, were found. The separation distance $[H1 \cdots H2]$ of 2.20 Å was found. The H₂ dissociative adsorption structure of the H₂/m-ZrO₂(111), one H atom was adsorbed on the Zr atom (Zr1) and one on two Zr atoms (Zr1 and Zr2) which is consistent with previous work [90], as shown in Figure 4.4(c) and the bond distances of $[Zr1-H1] = 1.91$, $[Zr1-H2] = 2.18$, and $[Zr2-H2] = 1.96$ Å, were found. The separation distance $[H1 \cdots H2]$ of 1.91 Å was found. H₂ adsorption on oxygen vacancy defective ZrO₂ surfaces exhibits similar in the dissociative chemisorption to previous work [91]. H₂ molecule are positioned close to oxygen vacancy on these oxygen vacancy defective surface which is corresponding to previous work [92]. The dissociative chemical adsorption on oxygen vacancy defective ZrO₂ surfaces inferred that H atom prefer to adsorb on oxygen vacancy defective ZrO₂ surfaces but does not for adsorption on pristine ZrO₂ surfaces. H₂ adsorption on oxygen vacancy defective ZrO₂ surfaces is dissociative chemical adsorption due to the deficient electron on surface which electron in H atom fulfill in this deficient.

The adsorption abilities of all the oxygen vacancy defective ZrO₂ surfaces on H₂ are in order: $[c-ZrO_2(111)+V_O]$ ($\Delta E_{ads} = -4.13$ eV) > $[m-ZrO_2(111)+V_O]$ ($\Delta E_{ads} = -3.31$ eV) > $[t-ZrO_2(101)+V_O]$ ($\Delta E_{ads} = -2.91$ eV), as shown in Table 4.2. The results can be concluded that the oxygen vacancy defective ZrO₂ surfaces tend to be used as hydrogen storage materials due to their H atom adsorption to form hydride which can be heating to release hydrogen [93].

Table 4.2 Adsorption energies (in eV) of a hydrogen molecule on the c-ZrO₂(111), t-ZrO₂(101), and m-ZrO₂(111) surfaces and their oxygen vacancy defect.

Systems	ΔE_{ads}^a
<i>Pristine:</i>	
H ₂ /c-ZrO ₂ (111)	-1.89
H ₂ /t-ZrO ₂ (101)	-0.27
H ₂ /m-ZrO ₂ (111)	-1.67
<i>V_O defective:</i>	
H ₂ /[c-ZrO ₂ (111)+V _O]	-4.13
H ₂ /[t-ZrO ₂ (101)+V _O]	-2.91
H ₂ /[m-ZrO ₂ (111)+V _O]	-3.31

^a In eV.

4.3 The charge transfers process on adsorption structures of polymorphic ZrO₂ surfaces

Charges and charge transfers over the Zr adsorption center of the c-ZrO₂(111), t-ZrO₂(101), and m-ZrO₂(111) and their oxygen vacancy defective surfaces during adsorptions are shown in Table 4.3. It shows that charge transfers over the Zr adsorption center of adsorption surfaces are in order: c-ZrO₂(111) ($\Delta q_{\text{Zr}} = -0.047 \text{ e}$) > m-ZrO₂(111) ($\Delta q_{\text{Zr}} = -0.041 \text{ e}$) > t-ZrO₂(101) ($\Delta q_{\text{Zr}} = -0.010 \text{ e}$) for the pristine ZrO₂ surfaces. For the oxygen vacancy defective ZrO₂ surfaces, the results show that charge transfers over the Zr adsorption center of adsorption surfaces are in order: [t-ZrO₂(101)+V_O] ($\Delta q_{\text{Zr}} = -0.002 \text{ e}$) > [m-ZrO₂(111)+V_O] ($\Delta q_{\text{Zr}} = 0.075 \text{ e}$) > [c-ZrO₂(111)+V_O] ($\Delta q_{\text{Zr}} = 0.127 \text{ e}$). Charges of the Zr adsorption center of H₂ adsorption on pristine ZrO₂ surfaces are in order: H₂/c-ZrO₂(111) ($q_{\text{Zr}} = 2.022 \text{ e}$) > H₂/m-ZrO₂(111) ($q_{\text{Zr}} = 1.917 \text{ e}$) > H₂/t-ZrO₂(101) ($q_{\text{Zr}} = 1.890 \text{ e}$) surfaces. Charges of the Zr adsorption center of H₂ adsorption on oxygen vacancy defective ZrO₂ surfaces are in order: H₂/[c-ZrO₂(111)+V_O] ($q_{\text{Zr}} = 2.006 \text{ e}$) > H₂/[t-ZrO₂(101)+V_O] ($q_{\text{Zr}} = 1.898 \text{ e}$) > H₂/[m-ZrO₂(111)+V_O] ($q_{\text{Zr}} = 1.830 \text{ e}$) surfaces. The Partial Mülliken–charge of H atom after adsorption on the oxygen vacancy defective ZrO₂ surfaces exhibit negative value

that can confirm homolytic dissociative adsorption on these surfaces which is corresponding to previous work [89, 92].

Table 4.3 The partial charge of the Zr adsorption-site atom, and its change after adsorption. of a hydrogen molecule on the c-ZrO₂(111), t-ZrO₂(101), and m-ZrO₂(111) surfaces and their oxygen vacancy defect.

Systems	q_{Zr}^{a}	$\Delta q_{\text{Zr}}^{\text{b}}$	q_{H1}^{a}	q_{H2}^{a}
<i>Pristine:</i>				
c-ZrO ₂ (111)	2.069	–	–	–
H ₂ /c-ZrO ₂ (111)	2.022	–0.047	–0.006	–0.012
t-ZrO ₂ (101)	1.900	–	–	–
H ₂ /t-ZrO ₂ (101)	1.890	–0.010	–0.013	–0.013
m-ZrO ₂ (111)	1.958	–	–	–
H ₂ /m-ZrO ₂ (111)	1.917	–0.041	–0.006	–0.009
<i>V_O defective:</i>				
[c-ZrO ₂ (111)+V _O]	1.879	–	–	–
H ₂ /[c-ZrO ₂ (111)+V _O]	2.006	0.127	–0.432	–0.543
[t-ZrO ₂ (101)+V _O]	1.900	–	–	–
H ₂ /[t-ZrO ₂ (101)+V _O]	1.898	–0.002	–0.451	–0.535
[m-ZrO ₂ (111)+V _O]	1.755	–	–	–
H ₂ /[m-ZrO ₂ (111)+V _O]	1.830	0.075	–0.400	–0.471

^a Partial Mülliken–charge of Zr atom, in e.

^b Change of partial Mülliken–charges of Zr atom, in e.

The partial Mülliken–charges of selected atoms on the pristine ZrO₂ surfaces, their H₂ adsorption complexes of which Zr (Zr1, Zr2, Zr3) and O (O1 to O4 or O6) that are around the adsorption site and changes of their charges are shown in Table 4.4. The results show that the charge transfers (Δq) during hydrogen adsorption on adsorption atom (Zr1) of the pristine ZrO₂ surfaces are found to be highest value.

The partial Mülliken–charges of selected atoms on the oxygen vacancy defective ZrO_2 surfaces, their H_2 adsorption complexes of which Zr (Zr1, Zr2, Zr3) and O (O1 to O4 or O6) that are around the adsorption site and changes of their charges are shown in Table 4.5. The results show that the charge transfers (Δq) during dissociative H_2 adsorption on adsorption atom (Zr2) of [t- $\text{ZrO}_2(101)+\text{Vo}$] and [m- $\text{ZrO}_2(111)+\text{Vo}$] and on adsorption atom (Zr1) of [c- $\text{ZrO}_2(111)+\text{Vo}$] are found to be the highest value. The charge transfer on Zr1 of [t- $\text{ZrO}_2(101)+\text{Vo}$] (Δq_{Zr1}) is slightly negative value ($-0.002 e$) which is rather to be neutral but other adsorption atom (Zr2 and Zr3) is high positive value. From the partial Mülliken–charges, it can be concluded that electron transfer directions are from O atom to Zr atom through O–Zr bond and Zr to H atom through Zr–H bond.



Table 4.4 Partial Mülliken–charges (in e) of selected atoms on the pristine ZrO₂ surfaces, their H₂ adsorption complexes, and changes of their charges (Δq).

Selected atom ^a	Clean surfaces	H ₂ adsorbed surfaces	Δq ^b
<i>c</i>-ZrO₂ surface:			
	c-ZrO ₂ (111)	H ₂ /c-ZrO ₂ (111)	
Zr1(Zr _{7C}) ^{c,d}	2.069	2.022	-0.047
Zr2(Zr _{7C}) ^c	2.069	2.035	-0.034
Zr3(Zr _{7C}) ^c	2.069	2.035	-0.034
O1(O _{3C}) ^e	-1.074	-1.062	0.012
O2(O _{3C}) ^e	-1.074	-1.062	0.012
O3(O _{3C}) ^e	-1.074	-1.063	0.011
O4(O _{3C}) ^f	-0.998	-0.963	0.035
O5(O _{3C}) ^f	-0.998	-0.964	0.034
O6(O _{3C}) ^f	-0.998	-0.963	0.035
<i>t</i>-ZrO₂ surface:			
	t-ZrO ₂ (101)	H ₂ /t-ZrO ₂ (101)	
Zr1(Zr _{6C}) ^{g,d}	1.900	1.890	-0.010
Zr2(Zr _{6C}) ^g	1.900	1.895	-0.005
Zr3(Zr _{6C}) ^g	1.900	1.895	-0.005
O1(O _{3C}) ^h	-0.964	-0.950	0.014
O2(O _{3C}) ^h	-0.952	-0.943	0.009
O3(O _{3C}) ^h	-0.964	-0.950	0.014
O4(O _{3C}) ⁱ	-1.019	-1.019	0.000
O5(O _{3C}) ⁱ	-0.972	-0.970	0.002
O6(O _{3C}) ⁱ	-0.972	-0.970	0.002
<i>m</i>-ZrO₂ surface:			
	m-ZrO ₂ (111)	H ₂ /m-ZrO ₂ (111)	
Zr1 (Zr _{6C}) ^{j,d}	1.958	1.917	-0.041
Zr2 (Zr _{7C}) ^j	1.921	1.893	-0.028
Zr3 (Zr _{7C}) ^j	1.921	1.893	-0.028
O1 (O _{2C}) ^k	-0.821	-0.798	0.023
O2 (O _{3C}) ^l	-0.952	-0.928	0.024
O3 (O _{3C}) ^m	-1.039	-1.009	0.030
O4 (O _{2C}) ⁿ	-0.909	-0.880	0.029

^a Labeled atoms are shown in Figure A–2 in Appendices.

^b Change of partial Mülliken–charges of selected atom in specific surfaces, in e, compared with a clean surface. ^c The L-2 layer for c-ZrO₂(111). ^d The adsorption site. ^e The L-1 layer for c-ZrO₂(111). ^f The L-3 layer for c-ZrO₂(111). ^g The L-1 layer for t-ZrO₂(101). ^h The L-2 layer for t-ZrO₂(101). ⁱ The L-3 layer for t-ZrO₂(101). ^j The L-5 layer for m-ZrO₂(111). ^k The L-1 layer for m-ZrO₂(111). ^l The L-2 layer for m-ZrO₂(111). ^m The L-3 layer for m-ZrO₂(111). ⁿ The L-4 layer for m-ZrO₂(111).

Table 4.5 Partial Mülliken–charges (in e) of selected atoms on the oxygen vacancy defective ZrO₂ surfaces, their H₂ adsorption complexes, and changes of their charges (Δq).

Selected atom ^a	Clean surfaces	H ₂ adsorbed surfaces	Δq ^b
[c-ZrO₂+V_O] surface:	[c-ZrO ₂ (111)+V _O]	H ₂ /[c-ZrO ₂ (111)+V _O]	
Zr1(Zr _{7C}) ^{c,d}	1.879	2.006	0.127
Zr2(Zr _{7C}) ^c	1.879	2.006	0.127
Zr3(Zr _{7C}) ^c	1.879	1.937	0.058
O1(O _{3C}) ^e	-1.030	-0.965	0.065
O2(O _{3C}) ^e	-1.030	-0.965	0.065
O3(O _{3C}) ^e	-1.030	-0.920	0.110
O4(O _{3C}) ^f	-1.166	-1.082	0.084
O5(O _{3C}) ^f	-1.166	-1.082	0.084
O6(O _{3C}) ^f	-1.073	-1.065	0.008
[t-ZrO₂+V_O] surface:	[t-ZrO ₂ (101)+V _O]	H ₂ /[t-ZrO ₂ (101)+V _O]	
Zr1(Zr _{6C}) ^{g,d}	1.900	1.898	-0.002
Zr2(Zr _{6C}) ^g	1.836	1.993	0.157
Zr3(Zr _{6C}) ^g	1.836	1.931	0.095
O1(O _{3C}) ^h	-0.976	-0.958	0.018
O2(O _{3C}) ^h	-1.015	-0.960	0.055
O3(O _{3C}) ^h	-0.976	-0.903	0.073
O4(O _{3C}) ⁱ	-1.100	-1.009	0.091
O5(O _{3C}) ⁱ	-1.052	-0.971	0.081
O6(O _{3C}) ⁱ	-1.052	-1.012	0.040
[m-ZrO₂+V_O] surface:	[m-ZrO ₂ (111)+V _O]	H ₂ /[m-ZrO ₂ (111)+V _O]	
Zr1 (Zr _{6C}) ^{j,d}	1.755	1.830	0.075
Zr2 (Zr _{7C}) ^j	1.724	1.954	0.230
Zr3 (Zr _{7C}) ^j	1.939	1.946	0.007
O1 (O _{2C}) ^k	-1.031	-0.949	0.082
O2 (O _{3C}) ^l	-0.996	-0.864	0.132
O3 (O _{3C}) ^m	-1.052	-1.025	0.027
O4 (O _{2C}) ⁿ	-1.048	-0.947	0.101

^a Labeled atoms are shown in Figure A–3 in Appendices.

^b Change of partial Mülliken–charges of selected atom in specific surfaces, in e, compared with a clean surface. ^c The L-2 layer for [c-ZrO₂(111)+V_O]. ^d The adsorption site. ^e The L-1 layer for [c-ZrO₂(111)+ V_O]. ^f The L-3 layer for [c-ZrO₂(111)+ V_O]. ^g The L-1 layer for [t-ZrO₂(101)+ V_O]. ^h The L-2 layer for [t-ZrO₂(101)+ V_O]. ⁱ The L-3 layer for [t-ZrO₂(101)+ V_O]. ^j The L-5 layer for [m-ZrO₂(111)+ V_O]. ^k The L-1 layer for [m-ZrO₂(111)+ V_O]. ^l The L-2 layer for [m-ZrO₂(111)+ V_O]. ^m The L-3 layer for [m-ZrO₂(111)+ V_O]. ⁿ The L-4 layer for [m-ZrO₂(111)+ V_O].

4.4 The difference of bandgap and electrical conductivity and resistivity of a hydrogen molecule adsorption on polymorphic ZrO₂ surfaces.

The band gaps of the pristine and oxygen vacancy defective polymorphic ZrO₂ surfaces are shown in Table 4.6. The previous work shows that band gap of t-ZrO₂ is larger than band gap of m-ZrO₂ (0.35 eV), which agreed with this work that band gap of t-ZrO₂ is larger than band gap of m-ZrO₂ (0.36 eV) [94]. The band gaps of all ZrO₂ surfaces are in order: c-ZrO₂ (111) ($E_{\text{gap}} = 3.44$ eV) > t-ZrO₂ (101) ($E_{\text{gap}} = 3.09$ eV) > m-ZrO₂ (111) ($E_{\text{gap}} = 2.73$ eV) > [c-ZrO₂(111)+V_O] ($E_{\text{gap}} = 0.48$ eV) > [t-ZrO₂(101)+V_O] ($E_{\text{gap}} = 0.39$ eV) > [m-ZrO₂(111)+V_O] ($E_{\text{gap}} = 0.23$ eV), as shown in Table 4.6. It can be concluded that the c-ZrO₂ (111) surface showed the lowest electrical conductivity compared with the t-ZrO₂ (101) and m-ZrO₂ (111) for pristine and oxygen vacancy defective surfaces.

Table 4.6 Energy gaps and sensitivity of electrical conductivity and resistivity of adsorption of hydrogen molecule on pristine and oxygen vacancy defective polymorphic ZrO₂ surfaces.

Systems	E_g^a	$\Delta E_g^{\%b}$	$S_{\sigma}^{\%}$ or $S_{\rho}^{\%c}$
<i>Pristine:</i>			
c-ZrO ₂ (111)	3.44	–	–
H ₂ /c-ZrO ₂ (111)	3.43	–0.23	$S_{\sigma}^{\%} = 21.5$
t-ZrO ₂ (101)	3.09	–	–
H ₂ /t-ZrO ₂ (101)	2.99	–3.09	$S_{\sigma}^{\%} = 600.0$
m-ZrO ₂ (111)	2.73	–	–
H ₂ /m-ZrO ₂ (111)	2.84	3.98	$S_{\rho}^{\%} = 750.4$
<i>V_O defective:</i>			
[c-ZrO ₂ (111)+V _O]	0.48	–	–
H ₂ /[c-ZrO ₂ (111)+V _O]	0.49	1.71	$S_{\rho}^{\%} = 21.5$
[t-ZrO ₂ (101)+V _O]	0.39	–	–
H ₂ /[t-ZrO ₂ (101)+V _O]	2.22	463.37	$S_{\rho}^{\%} = 2.9 \times 10^{17}$
[m-ZrO ₂ (111)+V _O]	0.23	–	–
H ₂ /[m-ZrO ₂ (111)+V _O]	1.21	439.29	$S_{\rho}^{\%} = 1.9 \times 10^{10}$

^a In eV.

^b Percentage of energy–gap change for hydrogen adsorbed on the surface compared with its clean surface.

^c Defined in equations (3.5) and (3.7).

The sensitivity of electrical conductivity ($S_{\sigma}^{\%}$) and resistivity ($S_{\rho}^{\%}$) of adsorption of hydrogen molecule on polymorphic ZrO₂ surfaces are shown in Table 4.6. The sensitivity of electrical conductivity of adsorption H₂ on surfaces are in order: t-ZrO₂(101) >> c-ZrO₂(111). The sensitivity of electrical resistivity of adsorption H₂ on surfaces are in order: [t-ZrO₂(101)+V_O] >> [m-ZrO₂(111)+V_O] >> m-ZrO₂(111) > [c-ZrO₂(111)+V_O]. It can be suggested that [t-ZrO₂(101)+V_O], [m-ZrO₂(111)+V_O], and m-ZrO₂(111) could be used as hydrogen sensing material via resistance measurement.

Table 4.7 shows energy gaps of pristine polymorphic ZrO₂ surfaces compared with their oxygen vacancy defects. Energy gaps of oxygen vacancy defective polymorphic ZrO₂ surfaces are much lower than pristine polymorphic ZrO₂ surfaces.

Table 4.7 Energy gaps of the c-ZrO₂(111), t-ZrO₂(101), and m-ZrO₂(111) surfaces compared with their oxygen vacancy defect in terms of energy–gap change.

Systems	E_g^a	$\Delta E_g^{\%}(\text{surface})^b$
c-ZrO ₂ (111)	3.44	–
[c-ZrO ₂ (111)+V _O]	0.48	–86.05
t-ZrO ₂ (101)	3.09	–
[t-ZrO ₂ (101)+V _O]	0.39	–87.38
m-ZrO ₂ (111)	2.73	–
[m-ZrO ₂ (111)+V _O]	0.23	–91.58

^a In eV.

^b Percentage of energy–gap change between the pristine ZrO₂ surface and its oxygen vacancy defect.

4.5 Bond strengths of adsorption of a hydrogen molecule on polymorphic ZrO₂ surfaces

Due to the hydrogen dissociative adsorption on oxygen vacancy defective polymorphic ZrO₂ surfaces, the relevant Zr–H bond strengths deserve further investigation. Table 4.8 shows the bond strengths of Zr–H bond resulted from hydrogen adsorption on oxygen vacancy defective polymorphic ZrO₂ surfaces. [c-ZrO₂(111)+V_O] shows the highest bond strength with –7.89 eV at Zr3–H1 bond.

Table 4.8 Zr-H bond strengths of a hydrogen molecule on oxygen vacancy defective ZrO₂ surfaces, computed by equation (3.8).

Parameters	q_X^a	Zr-H bond ^b	BS^c
H ₂ /[c-ZrO ₂ (111)+V _O]:			
Zr1	2.006	–	–
Zr2	2.006	–	–
Zr3	1.937	–	–
H1	-0.432	–	–
H2	-0.543	–	–
Zr1-H2	–	2.09	-5.97
Zr2-H2	–	2.09	-5.97
Zr3-H1	–	1.92	-7.89
H ₂ /[t-ZrO ₂ (101)+V _O]:			
Zr2	1.993	–	–
Zr3	1.931	–	–
Zr4	1.931	–	–
H1	-0.451	–	–
H2	-0.535	–	–
Zr2-H2	–	2.27	-6.76
Zr4-H2	–	2.03	-7.33
Zr3-H1	–	1.90	-6.60
H ₂ /[m-ZrO ₂ (111)+V _O]:			
Zr1	1.830	–	–
Zr2	1.954	–	–
H1	-0.400	–	–
H2	-0.471	–	–
Zr1-H1	–	1.91	-5.52
Zr1-H2	–	2.18	-5.69
Zr2-H2	–	1.96	-6.76

^a Atomic charge in e.

^b Bond length in Å.

^c Bond strength in eV.

4.6 Hydrogen adsorption on Lanthanide-doped c-ZrO₂(111) surface

The study of hydrogen adsorption on Lanthanide-doped c-ZrO₂(111) was investigated to compare with hydrogen adsorption on c-ZrO₂(111) surface. The optimized surfaces of c-ZrO₂(111) and Ce-[c-ZrO₂(111)] are shown in Figure A-6. Bond length of Ce-O which is on L-1 is 2.16 Å and Ce-O which is on L-3 is 2.22 Å. The total energies of c-ZrO₂(111), Ce-[c-ZrO₂(111)+V_o], [c-ZrO₂(111)+V_o], and Eu-[c-ZrO₂(111)+V_o] are shown in Table 4.9. The total energies of Ce-[c-ZrO₂(111)+V_o] is much lower than c-ZrO₂(111) but the total energies of Eu-[c-ZrO₂(111)+V_o] is higher than [c-ZrO₂(111)+V_o] due to the larger size of Eu³⁺ than Zr⁴⁺ on [c-ZrO₂(111)+V_o] surface. Adsorption of a hydrogen molecule on c-ZrO₂(111) surface compare with Ce-[c-ZrO₂(111)] surface structures are shown in Figure 4.5. The adsorption of a hydrogen molecule on Ce-[c-ZrO₂(111)] show the similar to the adsorption of a hydrogen molecule on c-ZrO₂(111) which is physisorption. H₂ adsorption on c-ZrO₂(111) and Ce-[c-ZrO₂(111)] is non-dissociative. The separation distance between H₂ and Ce-[c-ZrO₂(111)] is 2.93 and 2.86 Å. The adsorption energies of hydrogen molecule adsorption on Ce-[c-ZrO₂(111)] are shown in Table 4.10 with -0.21 eV which is lower than the adsorption energies of hydrogen molecule on c-ZrO₂(111). The change of charges of Ce dopant atom after hydrogen molecule adsorption on Ce-[c-ZrO₂(111)] (Δq_M) is slightly negative with -0.004 e. Since Ce doped on c-ZrO₂(111) is Ce³⁺ that substituted Zr⁴⁺ in surface, H₂ adsorb on Ce-[c-ZrO₂(111)] is reduced Ce³⁺ to Ce⁴⁺ which stable on ZrO₂ surface. The partial Mülliken-charges of selected atoms on the [c-ZrO₂(111)] and Ce-[c-ZrO₂(111)] surfaces are show in Table 4.11. The partial Mülliken-charges exhibit that electron transfer from H₂ to Ce-[c-ZrO₂(111)] surface is less than electron transfer to c-ZrO₂(111) surface.

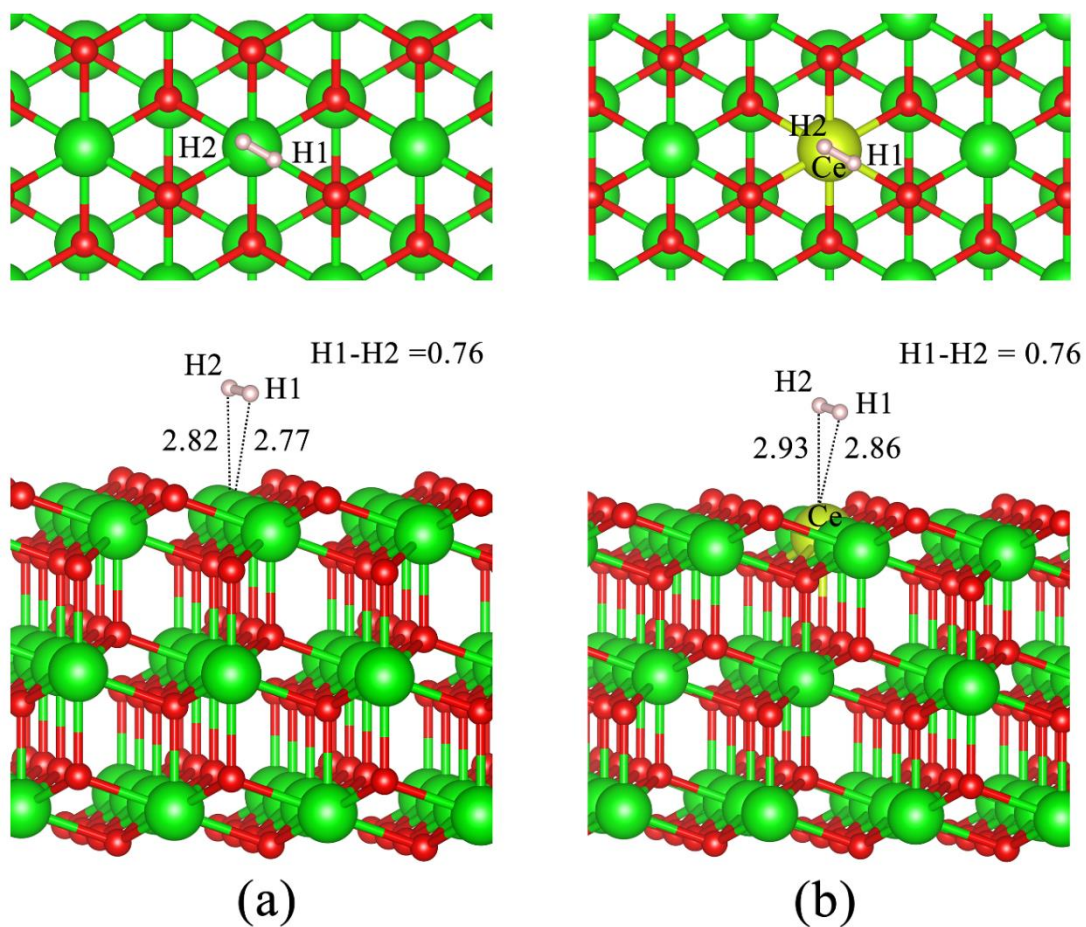


Figure 4.5 Optimized structures of hydrogen molecule adsorption on (a) $c\text{-ZrO}_2(111)$ and (b) $\text{Ce-[}c\text{-ZrO}_2(111)\text{]}$. The top and bottom panels are top and side views, respectively. The bond lengths of H-H and separation distance between hydrogen molecule and ZrO_2 surfaces are in Å.

Table 4.9 Total energies of the c-ZrO₂(111), Ce-[c-ZrO₂(101)], [c-ZrO₂(111)+V_o] and Eu-[c-ZrO₂(111)+V_o] surfaces.

Systems	E_{total}^a
c-ZrO ₂ (111)	-9467.52905449
Ce-[c-ZrO ₂ (101)]	-9896.02922386
c-ZrO ₂ (111)+V _o	-9392.13150240
Eu-[c-ZrO ₂ (111)+V _o]	-9380.97194800

^a In au. (1 Hartree = 27.2114 eV)

The optimized surfaces of [c-ZrO₂(111)+V_o] and Eu-[c-ZrO₂(111)+V_o] are shown in Figure A-6. Eu³⁺ substitute in Zr⁴⁺ in [c-ZrO₂(111)+V_o] surface. Bond length of Eu-O is 2.22 Å. Adsorption of a hydrogen molecule on Eu-[c-ZrO₂(111)+V_o] surface compare with a hydrogen molecule adsorption on [c-ZrO₂(111)+V_o] surface structures are shown in Figure 4.6. The H₂ adsorption on Eu-[c-ZrO₂(111)+V_o] is chemisorption which is similar to the H₂ adsorption on [c-ZrO₂(111)+V_o]. Nevertheless, H₂ molecule adsorbed on Eu-[c-ZrO₂(111)+V_o] is non-dissociative with bond length of [H-H] = 0.93 Å that is different from the H₂ adsorption on [c-ZrO₂(111)+V_o]. Hydrogen molecule adsorbs on Eu-[c-ZrO₂(111)+V_o] surface on top of Zr atom next to Eu dopant atom on surface. Bond distance between hydrogen molecule and Eu-[c-ZrO₂(111)+V_o] are 2.15 and 2.24 Å. The adsorption energies of hydrogen molecule adsorption on Eu-[c-ZrO₂(111)+V_o] are shown in Table 4.10. Adsorption energies of a hydrogen molecule on Eu-[c-ZrO₂(111)+V_o] are -0.80 eV which is much lower than H₂ adsorption energies on [c-ZrO₂(111)+V_o]. The change of charges of Eu atom doped on [c-ZrO₂(111)+V_o] surface after H₂ adsorption is positive with 0.115 e. The partial charges of H atom that are adsorbed on Eu-[c-ZrO₂(111)+V_o] surface is -0.303 and -0.115 e. The negative partial charges of H, Zr1, and Zr2 atom which are shown in Table 4.12 can be conclude that electron from H atom transfer to Zr atom on Eu-[c-ZrO₂(111)+V_o] that suggest being chemical bond on surface.

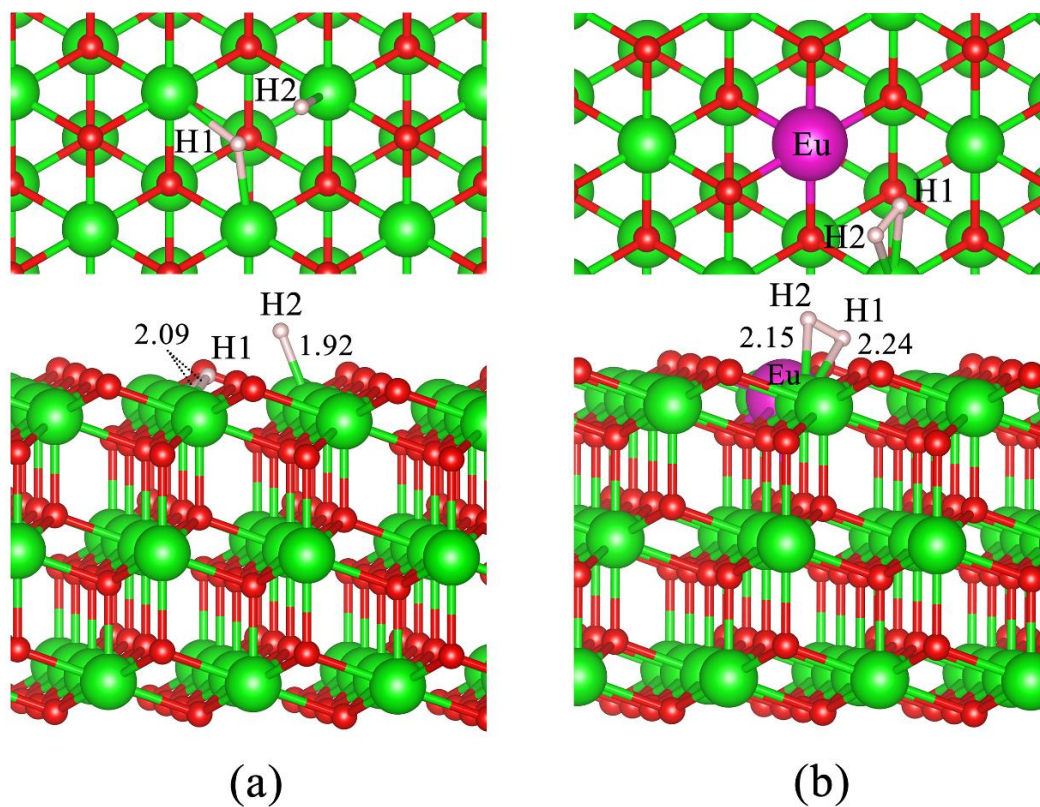


Figure 4.6 Optimized structures of hydrogen molecule adsorption on (a) [c-ZrO₂(111)+V_o] and (b) Eu-[c-ZrO₂(111)+V_o]. The top and bottom panels are top and side views, respectively. The bond lengths of H-H and separation distance between hydrogen molecule and ZrO₂ surfaces are in Å.

Table 4.10 Adsorption energies (in eV) of single H₂ molecules on the c-ZrO₂(111), Ce-[c-ZrO₂(101)], [c-ZrO₂(111)+V_O] and Eu-[c-ZrO₂(111)+V_O] surfaces, energy gaps, Mülliken charge of the dopant and Zr adsorption-site atoms and their change after hydrogen adsorption.

Systems	$\Delta E_{\text{ads}}^{\text{a}}$	E_{g}^{a}	$\Delta E_{\text{g}}^{\text{b}}$	q_{M}^{c}	$\Delta q_{\text{M}}^{\text{d}}$	q_{H1}^{e}	q_{H2}^{e}
c-ZrO ₂ (111)	–	3.44	–	2.069	–	–	–
H ₂ /c-ZrO ₂ (111)	–1.89	3.43	–0.23	2.022	–0.047	–0.006	–0.012
Ce-[c-ZrO ₂ (101)]	–	2.73	–	2.144	–	–	–
H ₂ /Ce-[c-ZrO ₂ (101)]	–0.21	2.75	0.85	2.140	–0.004	–0.014	–0.012
c-ZrO ₂ (111)+V _O	–	0.48	–	1.879	–	–	–
H ₂ /c-ZrO ₂ (111)+V _O	–4.13	0.49	1.71	2.006	0.127	–0.432	–0.543
Eu-[c-ZrO ₂ (111)+V _O]	–	2.71	–	1.612	–	–	–
H ₂ /Eu-[c-ZrO ₂ (111)+V _O]	–0.80	2.77	2.04	1.727	0.115	–0.303	–0.115

^a In eV.

^b Percentage of energy–gap change for hydrogen adsorbed on the surface compared with its clean surface.

^c Partial Mülliken–charge of dopant and Zr atom, in e.

^d Change of partial Mülliken–charges of dopant and Zr atom, in e.

^e Partial Mülliken–charge of H atom, in e.

Table 4.11 Partial Mülliken–charges (in e) of selected atoms on the [c-ZrO₂(111)] and Ce-[c-ZrO₂(111)] surfaces, their H₂ adsorption complexes and changes of their charges.

Selected atom ^a	Clean ZrO ₂ surfaces	H ₂ adsorption ZrO ₂ surfaces	Δq ^b
<i>c-ZrO₂(111) surface:</i>	<i>c-ZrO₂(111)</i>	<i>H₂/c-ZrO₂(111)</i>	
Zr1(Zr _{7C}) ^{c,d}	2.069	2.002	-0.047
Zr2(Zr _{7C}) ^c	2.069	2.035	-0.034
Zr3(Zr _{7C}) ^c	2.069	2.035	-0.034
O1(O _{3C}) ^e	-1.074	-1.062	0.012
O2(O _{3C}) ^e	-1.074	-1.062	0.012
O3(O _{3C}) ^e	-1.074	-1.063	0.011
O4(O _{3C}) ^f	-0.998	-0.963	0.035
O5(O _{3C}) ^f	-0.998	-0.964	0.034
O6(O _{3C}) ^f	-0.998	-0.963	0.035
<i>Ce-[c-ZrO₂(101)] surface:</i>	<i>Ce-[c-ZrO₂(101)]</i>	<i>H₂/Ce-[c-ZrO₂(101)]</i>	
Zr1(Zr _{6C}) ^{g,d}	2.031	2.030	-0.001
Ce(Ce _{6C}) ^g	2.144	2.140	-0.004
Zr3(Zr _{6C}) ^g	2.031	2.029	-0.002
O1(O _{3C}) ^h	-0.979	-0.969	0.010
O2(O _{3C}) ^h	-0.979	-0.965	0.014
O3(O _{3C}) ^h	-0.979	-0.969	0.010
O4(O _{3C}) ⁱ	-1.075	-1.075	0.000
O5(O _{3C}) ⁱ	-1.075	-1.075	0.000
O6(O _{3C}) ⁱ	-1.075	-1.075	0.000

^a Atomic labels are shown in Figure A–2 in Appendices.

^b Change of partial Mülliken–charges of selected atom in specific surfaces, in e, compared with clean surface. ^c The L-2 layer for c-ZrO₂(111). ^d The adsorption site. ^e The L-1 layer for c-ZrO₂(111). ^f The L-3 layer for c-ZrO₂(111). ^g The L-2 layer for Ce-[c-ZrO₂(111)]. ^h The L-1 layer for Ce-[c-ZrO₂(111)]. ⁱ The L-3 layer for Ce-[c-ZrO₂(111)].

Table 4.12 Partial Mülliken–charges (in e) of selected atoms on the [c-ZrO₂(111)+Vo] and Eu-[c-ZrO₂(111)+Vo] surfaces, their H₂ adsorption complexes and changes of their charges.

Selected atom ^a	Clean surfaces	H ₂ adsorbed surfaces	Δq ^b
[c-ZrO₂+Vo] surface:	[c-ZrO ₂ (111)+Vo]	H ₂ /[c-ZrO ₂ (111)+Vo]	
Zr1(Zr _{7C}) ^{c,d}	1.879	2.006	0.127
Zr2(Zr _{7C}) ^c	1.879	2.006	0.127
Zr3(Zr _{7C}) ^c	1.879	1.937	0.058
O1(O _{3C}) ^e	-1.030	-0.965	0.065
O2(O _{3C}) ^e	-1.030	-0.965	0.065
O3(O _{3C}) ^e	-1.030	-0.920	0.110
O4(O _{3C}) ^f	-1.166	-1.082	0.084
O5(O _{3C}) ^f	-1.166	-1.082	0.084
O6(O _{3C}) ^f	-1.073	-1.065	0.008
Eu-[c-ZrO₂+Vo] surface:	Eu-[c-ZrO ₂ +Vo]	H ₂ / Eu-[c-ZrO ₂ +Vo]	
Zr1(Zr _{6C}) ^{g,d}	1.891	1.910	0.019
Zr2(Zr _{6C}) ^g	2.039	1.946	-0.093
Eu(Eu _{6C}) ^g	1.612	1.727	0.115
O1(O _{3C}) ^h	-0.989	-0.977	0.012
O2(O _{3C}) ^h	-1.007	-0.952	0.055
O3(O _{3C}) ^h	-1.009	-0.973	0.036
O4(O _{3C}) ⁱ	-1.009	-0.988	0.021
O5(O _{3C}) ⁱ	-1.016	-1.017	-0.001
O6(O _{3C}) ⁱ	-1.006	-1.010	-0.004

^a Atomic labels are shown in Figure A–3 in Appendices.

^b Change of partial Mülliken–charges of selected atom in specific surfaces, in e, compared with clean surface. ^c The L-2 layer for [c-ZrO₂(111)+Vo]. ^d The adsorption site. ^e The L-1 layer for [c-ZrO₂(111)+Vo]. ^f The L-3 layer for [c-ZrO₂(111)+Vo]. ^g The L-2 layer for Eu-[c-ZrO₂(111)+Vo]. ^h The L-1 layer for Eu-[c-ZrO₂(111)+Vo]. ⁱ The L-3 layer for Eu-[c-ZrO₂(111)+Vo].

CHAPTER V

CONCLUSIONS

The hydrogen adsorption on the pristine and oxygen vacancy defective polymorphic ZrO_2 surfaces were investigated using a periodic DFT-D2 calculation method. This thesis covers the studies on geometrical stability, electric conductivity and resistivity, and charge transfer process of hydrogen adsorption on both surface types of ZrO_2 .

The c- ZrO_2 (111), t- ZrO_2 (101), and m- ZrO_2 (111) surfaces, and their oxygen vacancy defective surfaces [c- $\text{ZrO}_2(111)+\text{V}_\text{O}$], [t- $\text{ZrO}_2(101)+\text{V}_\text{O}$], and [m- $\text{ZrO}_2(111)+\text{V}_\text{O}$] were studied and found that their relative stabilities are in orders: c- $\text{ZrO}_2(111)$ ($\Delta E_{\text{rel}} = 0.00$ eV) > t- $\text{ZrO}_2(101)$ ($\Delta E_{\text{rel}} = 12.75$ eV) > m- $\text{ZrO}_2(111)$ ($\Delta E_{\text{rel}} = 13.91$ eV), and [c- $\text{ZrO}_2(111)+\text{V}_\text{O}$] ($\Delta E_{\text{rel}} = 0.00$ eV) > [t- $\text{ZrO}_2(101)+\text{V}_\text{O}$] ($\Delta E_{\text{rel}} = 12.05$ eV) > [m- $\text{ZrO}_2(111)+\text{V}_\text{O}$] ($\Delta E_{\text{rel}} = 12.82$ eV), respectively. The hydrogen adsorption energies of both surface types are in order: c- $\text{ZrO}_2(111)$ ($\Delta E_{\text{ads}} = -1.89$ eV) > m- $\text{ZrO}_2(111)$ ($\Delta E_{\text{ads}} = -1.67$ eV) > t- $\text{ZrO}_2(101)$ ($\Delta E_{\text{ads}} = -0.27$ eV), and [c- $\text{ZrO}_2(111)+\text{V}_\text{O}$] ($\Delta E_{\text{ads}} = -4.13$ eV), [m- $\text{ZrO}_2(111)+\text{V}_\text{O}$] ($\Delta E_{\text{ads}} = -3.31$ eV) > [t- $\text{ZrO}_2(101)+\text{V}_\text{O}$] ($\Delta E_{\text{ads}} = -2.91$ eV). Furthermore, the hydrogen adsorption ability on lanthanide-doped c- $\text{ZrO}_2(111)$ surfaces were obtained. Both of the hydrogen adsorption energies on Ce-[c- $\text{ZrO}_2(111)$] ($\Delta E_{\text{ads}} = -0.21$ eV) and on Eu-[c- $\text{ZrO}_2(111)+\text{V}_\text{O}$] ($\Delta E_{\text{ads}} = -0.80$ eV) are less than hydrogen adsorption energies on the pristine and oxygen vacancy defective c- $\text{ZrO}_2(111)$ surfaces.

The hydrogen adsorption abilities orders of the pristine and oxygen vacancy defective surfaces are consistent with the charge transfer on Zr adsorption center. The oxygen vacancy defective polymorphic ZrO_2 surfaces are suggested as potent materials for hydrogen storage. The m- $\text{ZrO}_2(111)+\text{V}_\text{O}$], [t- $\text{ZrO}_2(101)+\text{V}_\text{O}$], and m- $\text{ZrO}_2(111)$ surfaces are promising sensing materials for hydrogen based on their electrical resistances.

REFERENCES

- [1] A.M. Abdalla, S. Hossain, O.B. Nisfindy, A.T. Azad, M. Dawood, A.K. Azad, Hydrogen production, storage, transportation and key challenges with applications: A review, *Energy Conversion and Management*, 165 (2018) 602-627.
- [2] N.L. Garland, D.C. Papageorgopoulos, J.M. Stanford, Hydrogen and Fuel Cell Technology: Progress, Challenges, and Future Directions, *Energy Procedia*, 28 (2012) 2-11.
- [3] P. Jena, Materials for Hydrogen Storage: Past, Present, and Future, *The Journal of Physical Chemistry Letters*, 2 (2011) 206-211.
- [4] A. Züttel, Materials for hydrogen storage, *Materials Today*, 6 (2003) 24-33.
- [5] F.K. Butt, C. Cao, F. Idrees, M. Tahir, R. Hussain, R. Ahmed, W.S. Khan, Novel $Zn_2V_2O_7$ hierarchical nanostructures: Optical and hydrogen storage properties, *International Journal of Hydrogen Energy*, 40 (2015) 9359-9364.
- [6] W.G. Hong, B.H. Kim, S.M. Lee, H.Y. Yu, Y.J. Yun, Y. Jun, J.B. Lee, H.J. Kim, Agent-free synthesis of graphene oxide/transition metal oxide composites and its application for hydrogen storage, *International Journal of Hydrogen Energy*, 37 (2012) 7594-7599.
- [7] Z. Tarnawski, N.-T.H. Kim-Ngan, K. Zakrzewska, K. Drogowska, A. Brudnik, A.G. Balogh, R. Kužel, L. Havela, V. Sechovsky, Hydrogen storage in Ti-TiO₂ multilayers, *Advances in Natural Sciences: Nanoscience and Nanotechnology*, 4 (2013) 025004-025013.
- [8] Y. Yang, C.-S. Lin, W.-D. Cheng, Hydrogen adsorption induced antiferrodistortive distortion and metallization at the (001) surface of SrTiO₃, *Journal of Applied Physics*, 118 (2015) 105303-105311.
- [9] D.A. Ward, E.I. Ko, Synthesis and Structural Transformation of Zirconia Aerogels, *Chemistry of Materials*, 5 (1993) 956-969.
- [10] B. Sathyaseelan, E. Manikandan, I. Baskaran, K. Senthilnathan, K. Sivakumar, M.K. Moodley, R. Ladchumananandasivam, M. Maaza, Studies on structural and optical properties of ZrO₂ nanopowder for opto-electronic applications, *Journal of Alloys and Compounds*, 694 (2017) 556-559.
- [11] M. Hisbergues, S. Vendeville, P. Vendeville, Zirconia: Established facts and perspectives for a biomaterial in dental implantology, *Journal of Biomedical Materials Research Part B: Applied Biomaterials*, 88B (2009) 519-529.
- [12] S.P.S. Badwal, Ytria tetragonal zirconia polycrystalline electrolytes for solid state electrochemical cells, *Applied Physics A*, 50 (1990) 449-462.
- [13] E. Häfele, K. Kaltenmaier, U. Schönauer, Application of the ZrO₂ sensor in determination of pollutant gases, *Sensors and Actuators B: Chemical*, 4 (1991) 525-527.
- [14] Y. Kohno, T. Tanaka, T. Funabiki, S. Yoshida, Photoreduction of carbon dioxide with hydrogen over ZrO₂, *Chemical Communications*, (1997) 841-842.
- [15] G. Pacchioni, Ketonization of Carboxylic Acids in Biomass Conversion over TiO₂ and ZrO₂ Surfaces: A DFT Perspective, *ACS Catalysis*, 4 (2014) 2874-2888.
- [16] K. Tanabe, Surface and catalytic properties of ZrO₂, *Materials Chemistry and Physics*, 13 (1985) 347-364.
- [17] S. Tosoni, H.T. Chen, A. Ruiz Puigdollers, G. Pacchioni, TiO₂ and ZrO₂ in biomass conversion: why catalyst reduction helps, *Philos Trans A Math Phys Eng Sci*, 376 (2018) 20170056- 20170074.

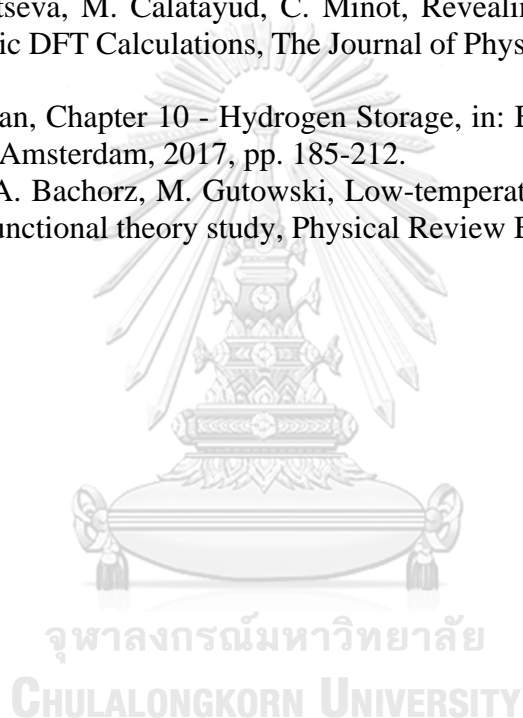
- [18] J.E. Jaffe, R.A. Bachorz, M. Gutowski, Low-temperature polymorphs of ZrO₂ and HfO₂: A density-functional theory study, *Physical Review B - Condensed Matter and Materials Physics*, 72 (2005) 144107-144115.
- [19] H.Y.T. Chen, S. Tosoni, G. Pacchioni, A DFT study of the acid–base properties of anatase TiO₂ and tetragonal ZrO₂ by adsorption of CO and CO₂ probe molecules, *Surface Science*, 652 (2016) 163-171.
- [20] Q.J. Liu, Z.T. Liu, L.P. Feng, Elasticity, electronic structure, chemical bonding and optical properties of monoclinic ZrO₂ from first-principles, *Physica B: Condensed Matter*, 406 (2011) 345-350.
- [21] Z. Liang, W. Wang, M. Zhang, F. Wu, J.F. Chen, C. Xue, H. Zhao, Structural, mechanical and thermodynamic properties of ZrO₂ polymorphs by first-principles calculation, *Physica B: Condensed Matter*, 511 (2017) 10-19.
- [22] J.T. Mazumder, R. Mayengbam, S.K. Tripathy, Theoretical investigation on structural, electronic, optical and elastic properties of TiO₂, SnO₂, ZrO₂ and HfO₂ using SCAN meta-GGA functional: A DFT study, *Materials Chemistry and Physics*, 254 (2020) 123474-123485.
- [23] M.A. Nazir, T. Mahmood, A.A. Zafar, N. Akhtar, T. Hussain, M.A. Saeed, F.E. Aleem, A. Saeed, J. Raza, C. Cao, Electronic, optical and elastic properties of cubic zirconia (c-ZrO₂) under pressure: A DFT study, *Physica B: Condensed Matter*, 604 (2021) 412462-412470.
- [24] J. Ouyang, J. Jin, X. Li, Z. Zhou, H. Yang, Electronic and optical properties of ZrO₂ and its applications, *Materials China*, 33 (2014) 497-505.
- [25] R. Guo, T. Liu, Y. Lu, Q. Li, X. Jiao, X. Xu, First-principles study on the optical spectra of ZrO₂ crystal with oxygen vacancy, *International Journal of Modern Physics B*, 33 (2019) 1950372- 1950382.
- [26] D.R. Islamov, V.A. Gritsenko, T.V. Perevalov, A.P. Yelisseyev, V.A. Pustovarov, I.V. Korolkov, E.E. Lomonova, Oxygen vacancies in zirconium oxide as the blue luminescence centres and traps responsible for charge transport: Part I—Crystals, *Materialia*, 15 (2021) 100979- 100984.
- [27] S. Jalili, M. Keshavarz, Zirconia (1 1 0) surface adsorption behavior – A density functional theory study, *Computational and Theoretical Chemistry*, 1173 (2020) 112702-112708.
- [28] Y.A. Mantz, R.S. Gemmen, Protonated forms of monoclinic zirconia: A theoretical study, *Journal of Physical Chemistry C*, 114 (2010) 8014-8025.
- [29] S.A. Tolba, N.K. Allam, Computational Design of Novel Hydrogen-Doped, Oxygen-Deficient Monoclinic Zirconia with Excellent Optical Absorption and Electronic Properties, *Scientific Reports*, 9 (2019) 10159- 10170.
- [30] G. Rajesh, S. Akilandeswari, D. Govindarajan, K. Thirumalai, Facile precipitation synthesis, structural, morphological, photoluminescence and photocatalytic properties of Ni doped ZrO₂ nanoparticles, *Materials Research Express*, 6 (2019) 1050a9.
- [31] E.F. de Souza, L.G. Appel, Oxygen vacancy formation and their role in the CO₂ activation on Ca doped ZrO₂ surface: An ab-initio DFT study, *Applied Surface Science*, 553 (2021) 149589- 149600.
- [32] Y. Liu, C. Xia, Q. Wang, L. Zhang, A. Huang, M. Ke, Z. Song, Direct dehydrogenation of isobutane to isobutene over Zn-doped ZrO₂ metal oxide heterogeneous catalysts, *Catalysis Science & Technology*, 8 (2018) 4916-4924.

- [33] M. Miyamoto, A. Hamajima, Y. Oumi, S. Uemiya, Effect of basicity of metal doped ZrO₂ supports on hydrogen production reactions, *International Journal of Hydrogen Energy*, 43 (2018) 730-738.
- [34] H.I. Song, J.A. Hong, H. Lee, K.I. Lim, Comparative study on the catalytic activity of Fe-doped ZrO₂ nanoparticles without significant toxicity through chemical treatment under various pH conditions, *Sci Rep*, 9 (2019) 10965-10977.
- [35] K. Gnanamoorthi, M. Balakrishnan, R. Mariappan, E. Ranjith Kumar, Effect of Ce doping on microstructural, morphological and optical properties of ZrO₂ nanoparticles, *Materials Science in Semiconductor Processing*, 30 (2015) 518-526.
- [36] L.X. Lovisa, V.D. Araújo, R.L. Tranquilin, E. Longo, M.S. Li, C.A. Paskocimas, M.R.D. Bomio, F.V. Motta, White photoluminescence emission from ZrO₂ co-doped with Eu³⁺, Tb³⁺ and Tm³⁺, *Journal of Alloys and Compounds*, 674 (2016) 245-251.
- [37] L.Y. Zhu, X.Q. Wang, G. Yu, X.Q. Hou, G.H. Zhang, J. Sun, X.J. Liu, D. Xu, Effect of Ce³⁺ doping and calcination on the photoluminescence of ZrO₂ (3% Y₂O₃) fibers, *Materials Research Bulletin*, 43 (2008) 1032-1037.
- [38] C. Gionco, M.C. Paganini, E. Giamello, O. Sacco, V. Vaiano, D. Sannino, Rare earth oxides in zirconium dioxide: How to turn a wide band gap metal oxide into a visible light active photocatalyst, *Journal of Energy Chemistry*, 26 (2017) 270-276.
- [39] S. Livraghi, M.C. Paganini, E. Giamello, G. Di Liberto, S. Tosoni, G. Pacchioni, Formation of Reversible Adducts by Adsorption of Oxygen on Ce-ZrO₂: An Unusual η² Ionic Superoxide, *The Journal of Physical Chemistry C*, 123 (2019) 27088-27096.
- [40] S. Manjunatha, M.S. Dharmaprakash, Synthesis and characterization of Cerium doped ZrO₂ blue-green emitting nanophosphors, *Materials Letters*, 164 (2016) 476-479.
- [41] N. García-Moncada, L.F. Bobadilla, R. Poyato, C. López-Cartes, F. Romero-Sarria, M.Á. Centeno, J.A. Odriozola, A direct in situ observation of water-enhanced proton conductivity of Eu-doped ZrO₂: Effect on WGS reaction, *Applied Catalysis B: Environmental*, 231 (2018) 343-356.
- [42] K. Srigurunathan, R. Meenambal, A. Guleria, D. Kumar, J. Ferreira, S. Kannan, Unveiling the Effects of Rare-Earth Substitutions on the Structure, Mechanical, Optical, and Imaging Features of ZrO₂ for Biomedical Applications, *ACS Biomater Sci Eng*, 5 (2019) 1725-1743.
- [43] C. Ricca, A. Ringuedé, M. Cassir, C. Adamo, F. Labat, Revealing the properties of the cubic ZrO₂ (111) surface by periodic DFT calculations: reducibility and stabilization through doping with aliovalent Y₂O₃, *RSC Advances*, 5 (2015) 13941-13951.
- [44] A.S. Bazhenov, K. Honkala, Understanding Structure and Stability of Monoclinic Zirconia Surfaces from First-Principles Calculations, *Topics in Catalysis*, 60 (2017) 382-391.
- [45] S. Dong, Y. Zhang, X. Zhang, J. Mao, Z. Yang, High Stability and Reactivity of Single-Metal Atom Catalysts Supported on Ytria-Stabilized Zirconia: The Role of the Surface Oxygen Vacancy, *Journal of Physical Chemistry C*, 122 (2018) 1622-1630.
- [46] G.R. Lumpkin, Physical and chemical characteristics of baddeleyite (monoclinic zirconia) in natural environments: an overview and case study, *Journal of Nuclear Materials*, 274 (1999) 206-217.
- [47] D.K. Smith, Newkirk, W., The crystal structure of baddeleyite (monoclinic ZrO₂) and its relation to the polymorphism of ZrO₂, *Acta Crystallographica*, 18 (1965) 983-991.
- [48] F.J. Mompean, J. Perrone, M. Illemassène, *Chemical Thermodynamics of Zirconium*, Elsevier Science 2005.

- [49] J. Park, *Bioceramics: Properties, Characterizations, and Applications*, Springer New York 2009.
- [50] K.S. Mazdiyasi, C.T. Lynch, J.S.S. Li, Cubic Phase Stabilization of Translucent Yttria-Zirconia at Very Low Temperatures, *Journal of the American Ceramic Society*, 50 (1967) 532-537.
- [51] T.E. Fischer, M.P. Anderson, S. Jahanmir, Influence of Fracture Toughness on the Wear Resistance of Yttria-Doped Zirconium Oxide, *Journal of the American Ceramic Society*, 72 (1989) 252-257.
- [52] T.K. Gupta, J.H. Bechtold, R.C. Kuznicki, L.H. Cadoff, B.R. Rossing, Stabilization of tetragonal phase in polycrystalline zirconia, *Journal of Materials Science*, 12 (1977) 2421-2426.
- [53] C. Ricca, A. Ringuede, M. Cassir, C. Adamo, F. Labat, A comprehensive DFT investigation of bulk and low-index surfaces of ZrO₂ polymorphs, *J Comput Chem*, 36 (2015) 9-21.
- [54] G. Katz, X-Ray Diffraction Powder Pattern of Metastable Cubic ZrO₂, *Journal of the American Ceramic Society*, 54 (1971) 531-531.
- [55] R. Orlando, C. Pisani, C. Roetti, E. Stefanovich, Ab initio Hartree-Fock study of tetragonal and cubic phases of zirconium dioxide, *Physical Review B*, 45 (1992) 592-601.
- [56] C. Morterra, G. Cerrato, L. Ferroni, A. Negro, L. Montanaro, Surface characterization of tetragonal ZrO₂, *Applied Surface Science*, 65-66 (1993) 257-264.
- [57] J.D. McCullough, K.N. Trueblood, The crystal structure of baddeleyite (monoclinic ZrO₂), *Acta Crystallographica*, 12 (1959) 507-511.
- [58] G. Cerrato, S. Bordiga, S. Barbera, C. Morterra, A surface study of monoclinic zirconia (m-ZrO₂), *Surface Science*, 377-379 (1997) 50-55.
- [59] W. Piskorz, J. Gryboś, F. Zasada, S. Cristol, J.-F. Paul, A. Adamski, Z. Sojka, Periodic DFT and Atomistic Thermodynamic Modeling of the Surface Hydration Equilibria and Morphology of Monoclinic ZrO₂ Nanocrystals, *The Journal of Physical Chemistry C*, 115 (2011) 24274-24286.
- [60] K. Pokrovski, K.T. Jung, A.T. Bell, Investigation of CO and CO₂ Adsorption on Tetragonal and Monoclinic Zirconia, *Langmuir*, 17 (2001) 4297-4303.
- [61] M. Kogler, E.M. Kock, T. Bielz, K. Pfaller, B. Klotzer, D. Schmidmair, L. Perfler, S. Penner, Hydrogen Surface Reactions and Adsorption Studied on Y₂O₃, YSZ, and ZrO₂, *J Phys Chem C Nanomater Interfaces*, 118 (2014) 8435-8444.
- [62] Y.-L. Yang, X.-L. Fan, C. Liu, R.-X. Ran, First principles study of structural and electronic properties of cubic phase of ZrO₂ and HfO₂, *Physica B: Condensed Matter*, 434 (2014) 7-13.
- [63] C. Gionco, M.C. Paganini, M. Chiesa, S. Maurelli, S. Livraghi, E. Giamello, Cerium doped zirconium dioxide as a potential new photocatalytic material. The role of the preparation method on the properties of the material, *Applied Catalysis A: General*, 504 (2015) 338-343.
- [64] A. Sinhamahapatra, J.P. Jeon, J. Kang, B. Han, J.S. Yu, Oxygen-Deficient Zirconia (ZrO_{2-x}): A New Material for Solar Light Absorption, *Sci Rep*, 6 (2016) 27218-27225.
- [65] M. Raza, D. Cornil, J. Cornil, S. Lucas, R. Snyders, S. Konstantinidis, Oxygen vacancy stabilized zirconia (OVSZ); a joint experimental and theoretical study, *Scripta Materialia*, 124 (2016) 26-29.
- [66] E.M. Kock, M. Kogler, B. Klotzer, M.F. Noisternig, S. Penner, Structural and Electrochemical Properties of Physisorbed and Chemisorbed Water Layers on the

- Ceramic Oxides Y_2O_3 , YSZ, and ZrO_2 , *ACS Appl Mater Interfaces*, 8 (2016) 16428-16443.
- [67] A. Ruiz Puigdollers, F. Illas, G. Pacchioni, Reduction of Hydrogenated ZrO_2 Nanoparticles by Water Desorption, *ACS Omega*, 2 (2017) 3878-3885.
- [68] T. Engel, P. Reid, *Physical Chemistry*, Pearson Education 2012.
- [69] I.N. Levine, *Quantum Chemistry*, Pearson Education 2013.
- [70] C.J. Cramer, *Essentials of Computational Chemistry: Theories and Models*, Wiley 2013.
- [71] E.G. Lewars, *Computational Chemistry: Introduction to the Theory and Applications of Molecular and Quantum Mechanics*, Springer, Cham 2016.
- [72] G.L. Miessler, P.J. Fischer, D.A. Tarr, *Inorganic Chemistry*, Pearson 2014.
- [73] S. Grimme, Semiempirical GGA-type density functional constructed with a long-range dispersion correction, *J. Comput. Chem.*, 27 (2006) 1787-1799.
- [74] J.P. Perdew, K. Burke, M. Ernzerhof, Generalized gradient approximation made simple, *Phys Rev Lett*, 77 (1996) 3865-3868.
- [75] S.V. Dovesi R, Roetti C, Orlando R, Zicovich-Wilson CM, Pascale F, et al., *CRYSTAL14 User's Manual*, The University of Torino, (2016).
- [76] T. Bredow, M. Lerch, Anion distribution in Zr_2ON_2 , *Z. Anorg. Allg. Chem.*, 630 (2004) 2262-2266.
- [77] J. Scaranto, S. Giorgianni, A quantum-mechanical study of CO adsorbed on TiO_2 : A comparison of the Lewis acidity of the rutile (110) and the anatase (101) surfaces, *J. Mol. Struct. THEOCHEM*, 858 (2008) 72-76.
- [78] R. Panta, V. Ruangpornvisuti, Unusual adsorption behavior of hydrogen molecules on Zr-doped perfect and oxygen-vacancy defective rutile $\text{TiO}_2(110)$ surfaces: Periodic DFT study, *International Journal of Hydrogen Energy*, 44 (2019) 32101-32111.
- [79] R. Dovesi, C. Ermondi, E. Ferrero, C. Pisani, C. Roetti, Hartree-Fock study of lithium hydride with the use of a polarizable basis set, *Physical Review B*, 29 (1984) 3591-3600.
- [80] J. Graciani, A.M. Márquez, J.J. Plata, Y. Ortega, N.C. Hernández, A. Meyer, C.M. Zicovich-Wilson, J.F. Sanz, Comparative Study on the Performance of Hybrid DFT Functionals in Highly Correlated Oxides: The Case of CeO_2 and Ce_2O_3 , *Journal of Chemical Theory and Computation*, 7 (2011) 56-65.
- [81] G. Katz, X-Ray Diffraction Powder Pattern of Metastable Cubic ZrO_2 , *J Am Ceram Soc*, 54 (1971) 531-531.
- [82] A. Taoudi, J.P. Laval, B. Frit, Synthesis and crystal structure of three new rare earth oxyfluorides related to baddeleyite [LnOF ; $\text{Ln}=\text{Tm}, \text{Yb}, \text{Lu}$], *Mater Res Bull*, 29 (1994) 1137-1147.
- [83] K. Momma, F. Izumi, VESTA 3 for three-dimensional visualization of crystal, volumetric and morphology data, *J. Appl. Crystallog.*, 44 (2011) 1272-1276.
- [84] C. Kittel, *Introduction to Solid State Physics*, John Wiley & Sons Inc 1976.
- [85] R.S. Christy, J.T.T. Kumaran, C. Bansal, M. Brightson, Phase transitions in $\text{CuS-Ag}_2\text{S}$ nanoparticle system, *Phase Transitions*, 89 (2015) 155-166.
- [86] R.L. Kumawat, M.K. Jena, B. Pathak, Individual Identification of Amino Acids on an Atomically Thin Hydrogen Boride System Using Electronic Transport Calculations, *Journal of Physical Chemistry C*, (2020) 27194-27202.
- [87] O. Vinogradov, Coulomb's law based interatomic potential for iron crystals in molecular statics applications, *Computational Materials Science*, 99 (2015) 173-176.

- [88] A. Hofmann, S.J. Clark, M. Oppel, I. Hahndorf, Hydrogen adsorption on the tetragonal $\text{ZrO}_2(101)$ surface: a theoretical study of an important catalytic reactant, *Physical Chemistry Chemical Physics*, 4 (2002) 3500-3508.
- [89] O. Syzgantseva, M. Calatayud, C. Minot, Hydrogen Adsorption on Monoclinic ($\bar{1}11$) and ($\bar{1}01$) ZrO_2 Surfaces: A Periodic ab Initio Study, *The Journal of Physical Chemistry C*, 114 (2010) 11918-11923.
- [90] T. Onishi, H. Abe, K.-i. Maruya, K. Domen, I.r. spectra of hydrogen adsorbed on ZrO_2 , *Journal of the Chemical Society, Chemical Communications*, (1985) 617-618.
- [91] Y. Hinuma, T. Toyao, T. Kamachi, Z. Maeno, S. Takakusagi, S. Furukawa, I. Takigawa, K.-i. Shimizu, Density Functional Theory Calculations of Oxygen Vacancy Formation and Subsequent Molecular Adsorption on Oxide Surfaces, *The Journal of Physical Chemistry C*, 122 (2018) 29435-29444.
- [92] O.A. Syzgantseva, M. Calatayud, C. Minot, Revealing the Surface Reactivity of Zirconia by Periodic DFT Calculations, *The Journal of Physical Chemistry C*, 116 (2012) 6636-6644.
- [93] B. Viswanathan, Chapter 10 - Hydrogen Storage, in: B. Viswanathan (Ed.) *Energy Sources*, Elsevier, Amsterdam, 2017, pp. 185-212.
- [94] J.E. Jaffe, R.A. Bachorz, M. Gutowski, Low-temperature polymorphs of ZrO_2 and HfO_2 : A density-functional theory study, *Physical Review B*, 72 (2005) 144107-144115.





APPENDICES

จุฬาลงกรณ์มหาวิทยาลัย
CHULALONGKORN UNIVERSITY

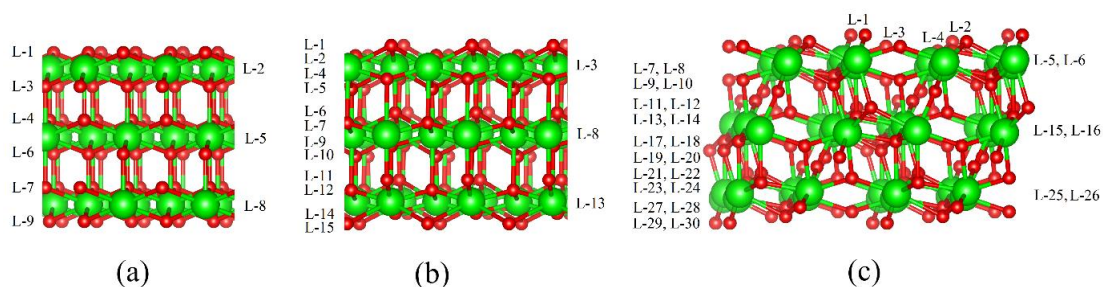


Figure A-1 The atomic layers assigned for the surfaces of the (a) c-ZrO₂(111), (b) t-ZrO₂(101), and (c) m-ZrO₂(111) surfaces. The L-n, n=1 to 30, is the nth layers.

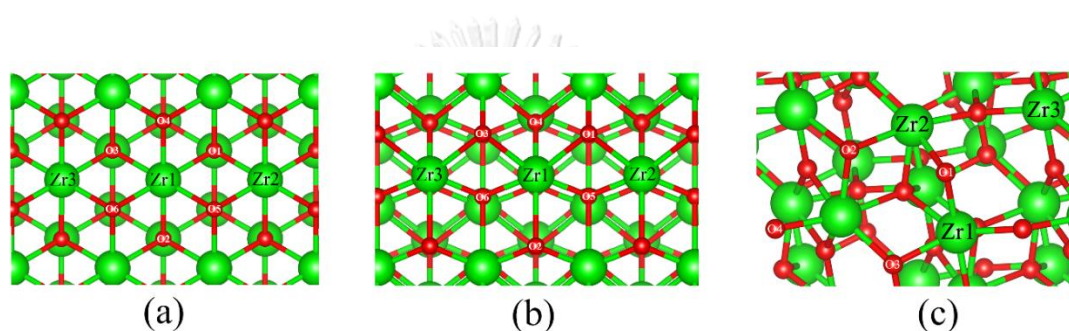


Figure A-2 The labeled atoms of the surfaces of the (a) c-ZrO₂(111), (b) t-ZrO₂(101), and (c) m-ZrO₂(111) surfaces.

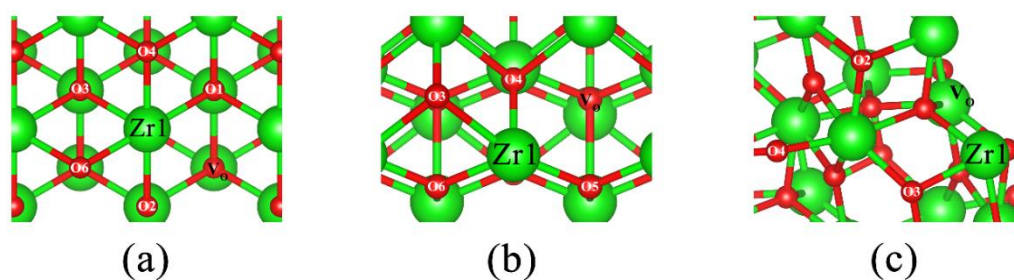


Figure A-3 The labeled atoms of the surfaces of the oxygen vacancy defective (a) c-ZrO₂(111), (b) t-ZrO₂(101), and (c) m-ZrO₂(111) surfaces.

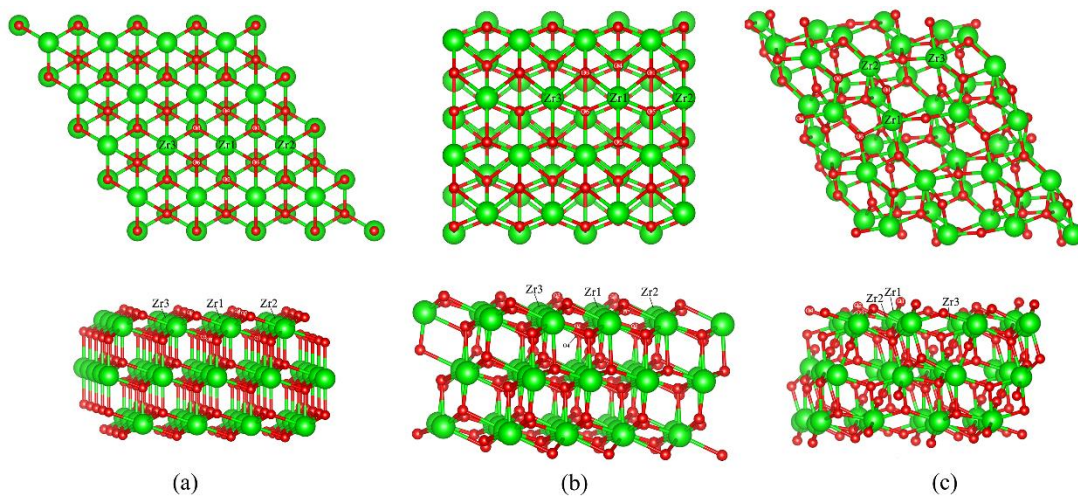


Figure A-4 Structures of (a) (4x4) c-ZrO₂(111), (b) (4x2) t-ZrO₂(101), and (c) (2x) m-ZrO₂(111) surfaces. The top and bottom panels show the top and side views, respectively.

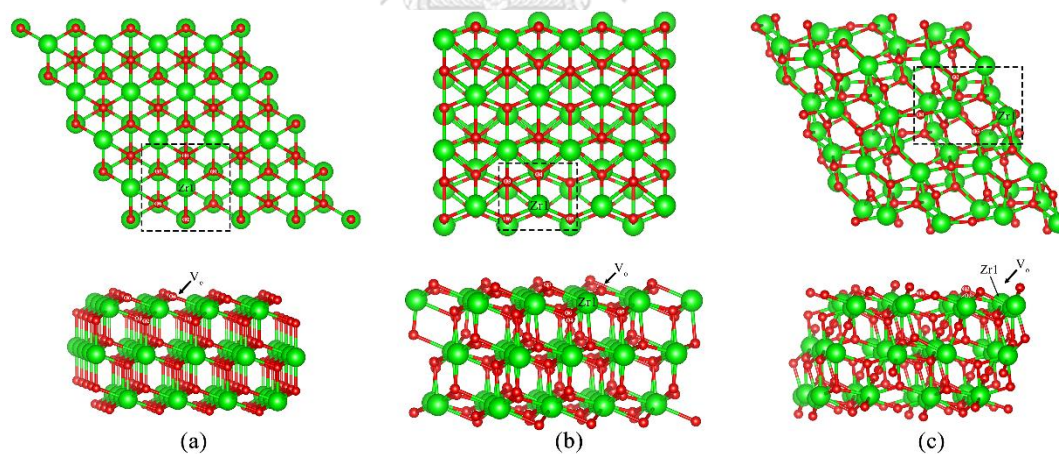


Figure A-5 Structures of (a) (4x4) [c-ZrO₂(111)+Vo], (b) (4x2) [t-ZrO₂(101) Vo], and (c) (2x2) [m-ZrO₂(111)+Vo] surfaces. The top and bottom panels show the top and side views, respectively. Vo indicates the oxygen vacancy. The rectangular areas (black dashed lines) indicate oxygen vacancy on these surfaces.

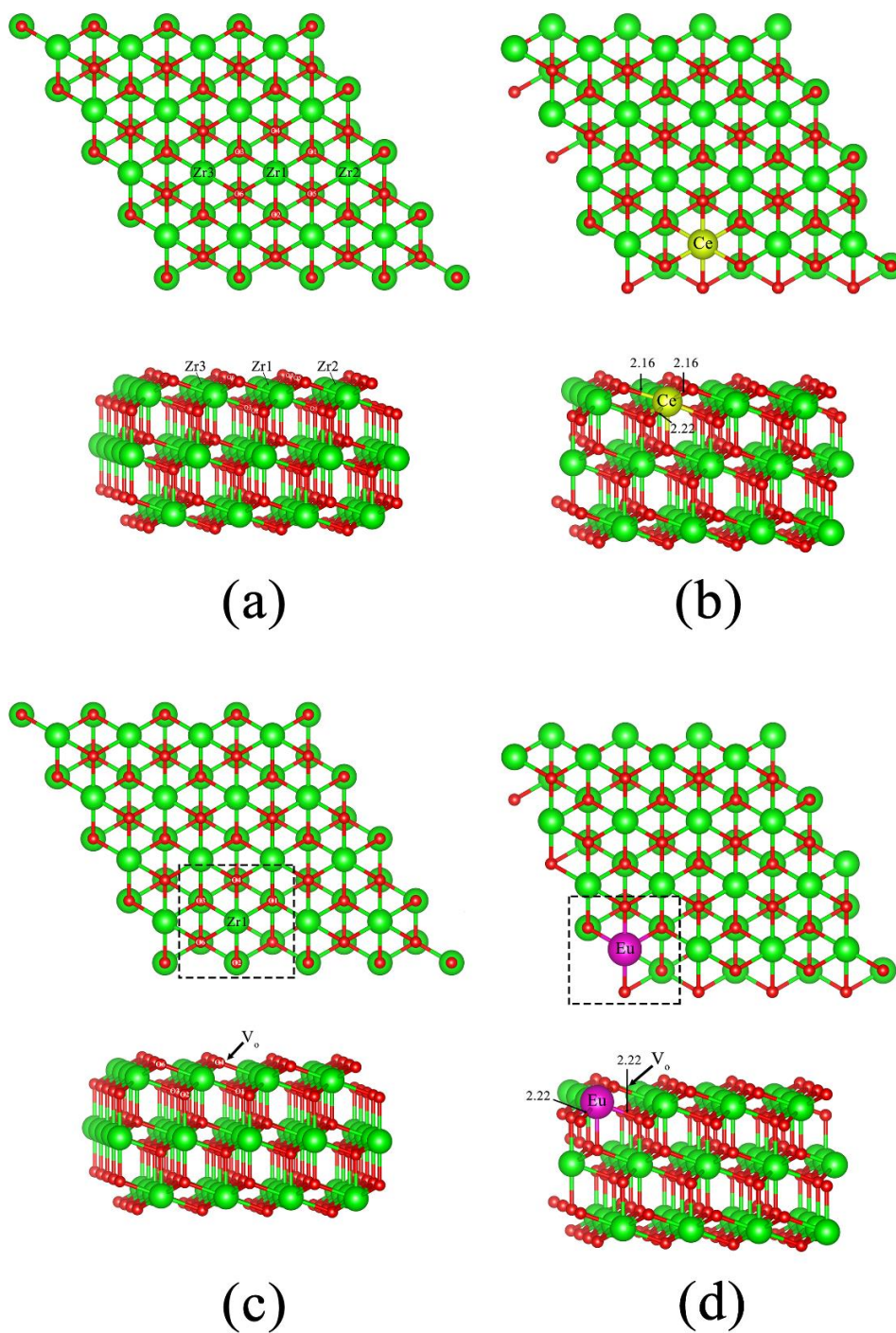


Figure A-6 Structure of (a) $c\text{-ZrO}_2(111)$, (b) $\text{Ce-}[c\text{-ZrO}_2(111)]$, (c) $[c\text{-ZrO}_2(111)+V_o]$, and (d) $\text{Eu-}[c\text{-ZrO}_2(111)+V_o]$ surfaces. The top and bottom panels are top and side views, respectively. The bond length between dopant and surface are in Å.

Table A–1 The Grimme, D2 parameters of the London-type empirical correction for dispersion interactions of all the elements used in this work.

Elements	C_6^a	R_{vdw}^b
$s_6 = 0.75^c$, $d = 20.0^d$, $R_{cut} = 25.0^e$		
Surfaces:		
Zr	24.67	1.639
O	0.70	1.342
Adsorbate:		
H	0.14	1.001
Dopants		
Ce	140.68	1.753
Eu	140.68	1.753

^a dispersion coefficient for atom in $\text{J nm}^6 \text{mol}^{-1}$.

^b Van der Waals radius for atom, in \AA .

^c Scaling factor.

^d Steepness.

^e Cutoff distance to truncate direct lattice summation.

Table A–2 The lattice parameters of the c-ZrO₂, t-ZrO₂ and m-ZrO₂ from x-ray crystallographic and their DFT optimized structures.

Crystals	Space group, Structural form	Lattice parameters ^a							
		X-ray ^b				DFT			
		<i>a</i>	<i>b</i>	<i>c</i>	β	<i>a</i>	<i>b</i>	<i>c</i>	β
c-ZrO ₂	$Fm\bar{3}m$, cubic	5.090				5.120			
t-ZrO ₂	$P4_2/nmc$, tetragonal	3.558	5.258			3.622	5.205		
m-ZrO ₂	$P2_1/c$, monoclinic	5.169	5.232	5.341	99.2	5.150	5.287	5.295	98.0

^a The *a*, *b*, and *c* parameters are in \AA , and β is in degree.

^b The c-ZrO₂, t-ZrO₂, and m-ZrO₂ were taken from refs. [81], [55], and [82], respectively.

Table A–3 Selected geometrical parameters of the clean *c*-ZrO₂(111), *t*-ZrO₂(101), *m*-ZrO₂(111) surfaces.

Crystal Forms	Bond length ^a	Bond angle ^b
<i>c</i>-ZrO₂(111)		
Zr1-Zr2, Zr1-Zr3	3.620	-
Zr1-O1, Zr1-O2, Zr1-O3	2.217	-
Zr1-O4, Zr1-O5, Zr1-O6	2.217	-
Zr1-O1-Zr2, Zr1-O3-Zr3	-	109.47
<i>t</i>-ZrO₂(101)		
Zr1-Zr2, Zr1-Zr3	3.622	-
Zr1-O1, Zr1-O2, Zr1-O3	2.482	-
Zr1-O4, Zr1-O5, Zr1-O6	2.025	-
Zr1-O1-Zr2, Zr1-O3-Zr3	-	93.73
O1-Zr1-O3	-	93.73
O5-Zr1-O6	-	126.86
O1-Zr1-O2, O2-Zr1-O3,	-	117.87
O4-Zr1-O5, O4-Zr1-O6	-	101.54
<i>m</i>-ZrO₂(111)		
Zr1-Zr2	3.453	-
Zr2-Zr3	3.948	-
Zr2-O1	2.160	-
Zr1-O1	2.100	-
Zr1-O3	2.164	-
Zr2-O2	2.256	-
O1-Zr1-O3	-	98.46
O2-Zr2-O1	-	84.52

^a In Å.

^b In degree.



VITA

- NAME** Monrada Petchmark
- DATE OF BIRTH** 10 August 1996
- PLACE OF BIRTH** Phatthalung, Thailand
- INSTITUTIONS ATTENDED**
- | | |
|-----------|---|
| 2019-2021 | M.Sc. in Physical chemistry, Chulalongkorn University, Thailand |
| 2015-2018 | B.Sc. in Chemistry, Chulalongkorn University, Thailand |
| 2009-2014 | Phatthalung School, Phatthalung, Thailand |
- PUBLICATION**
1. Petchmark, M.; Ruangpornvisuti, V., Adsorption of nitrosamine conformers on the C₂₄, B₁₂N₁₂, Be₁₂O₁₂ and Al₁₂P₁₂ nanocages and their conversion to nitrogen and water molecules: A DFT study. *Physica E: Low-dimensional Systems and Nanostructures* 2021, 127.
 2. Petchmark, M.; Ruangpornvisuti, V., Hydrogen adsorption on c-ZrO₂(111), t-ZrO₂(101), and m-ZrO₂(111) surfaces and their oxygen-vacancy defect for hydrogen sensing and storage: A first-principles investigation. *Materials Letters* 2021, 301.